# NUMERICAL MODELLING OF ULTRA-THIN STRUCTURES IN A FLUID DOMAIN

Varakini Sanmugadas

178083H

Degree of Master of Science

Department of Civil Engineering

University of Moratuwa

Sri Lanka

September 2018

# NUMERICAL MODELLING OF ULTRA-THIN STRUCTURES IN A FLUID DOMAIN

Varakini Sanmugadas

178083H

Thesis submitted in partial fulfilment of the requirements for the degree Master of Science in Civil Engineering

Department of Civil Engineering

University of Moratuwa

Sri Lanka

September 2018

## DECLARATION

I declare that this is my own work and this thesis does not incorporate without acknowledgement any material previously submitted for a Degree or Diploma in any other University or institute of higher learning and to the best of my knowledge and belief it does not contain any material previously published or written by another person except where the acknowledgement is made in the text.

Also, I hereby grant to University of Moratuwa the non-exclusive right to reproduce and distribute my thesis, in whole or in part in print, electronic or other medium. I retain the right to use this content in whole or part in future works (such as articles or books)

…… Date:

S.Varakini

The above candidate has carried out research for the Masters under my supervision.

…… Date:

Dr. H.M.Y.C. Mallikarachchi

# ABSTRACT

Folding structures with a large surface area into a compact configuration and deploying them only when required can be achieved by employing origami based folding patterns. This technique is widely seen in nature and mimicking such mechanisms for folding and deployment purposes can lead to highly efficient systems. This study focuses on the biomimicry of insect wings in the design of wings for insect-sized micro air vehicles (MAVs). In order to achieve the required aerodynamic lift and forward propulsion, the wings have to be sufficiently large. At the same time, for manoeuvrability while on ground and also to protect the wings while not in use, the size can be a limiting factor. The wing-folding technique used by certain class of insects is an attractive design solution, which however leads to the need for rigorous numerical analysis, as the fold lines introduced for folding purposes can alter the aerodynamic behaviour of the structure. For a comprehensive analysis a fluid structure interaction (FSI) framework will be required.

This thesis presents a detailed study of how the capabilities of commercially available computational structural dynamics (CSD) and computational fluid dynamics (CFD) codes can be exploited in conducting a FSI study of a system involving thin, creased, membranous structures immersed in flowing fluid. For this purpose, initially the suitability of two widely used software environments, ABAQUS and ANSYS Workbench, was investigated. Based on requirements and resource availability ABAQUS CAE and CFD solvers were chosen for the current work and a rigorous study of the theoretical concepts employed by these codes was conducted to ensure that it was in line with the objective at hand.

The FSI framework was implemented in three stages. First, the structural domain was developed. A Mooney-Rivlin material model with a membrane formulation was found to be suitable for modelling thin biological membranes. However, for simplicity a linear elastic material with plastic properties was initially assumed and was used in combination with a shell formulation.

Next, the fluid domain was developed using a Spalart-Allmaras turbulence model and was verified qualitatively based on the variation in flow around a rigid cylinder with Reynolds Number. Finally, both aforementioned domains were coupled using an explicit Gauss-Seidal scheme through the Abaqus Co-simulation Engine. This was verified against a standard benchmark study conducted by Turek and Hron (2006), which involves a cylinder immersed in a laminar flow with a thin, flexible flap attached to its downstream side. The sinusoidal oscillation of the flexible flap was captured and features such as vortices and streamlines were reproduced to an acceptable extent. However, the numerical accuracy of the solutions needs further improvement.

As the next stage, the behaviour of a creased membrane immersed in the above fluid domain was studied. To introduce the crease effect, the crease geometry was pre-defined on the structural component and this was then coupled with a fluid domain set up following the same procedure as in the previous case. This method, while presenting a simpler modelling path, has the disadvantage that the exact hinge-effect introduced by an actual crease-line is not captured. However, the alteration to the flow path from a geometric perspective was captured.

In the developed model a main concern was the processing time. To address this issue a two-dimensional shell formulation was used in this work. The presence of the shell was indicated by a seam crack in the fluid domain. Despite that, the model still suffered from the severe disadvantage of processing time. Thus in future works, other techniques should be incorporated to overcome this constraint. Also, the actual behaviour of the crease-line and the region close to it should be captured. A technique that could be used in future works was presented in the final section of the thesis.

**Key words:** Fluid structure interactions; Origami; Biomimicry; Deployable wings; Abaqus co-simulation engine

## DEDICATION

To my parents and sister for being with me at each step of my life and my supervisor, Dr.H.M.Y.C. Mallikarachchi, for his infectious enthusiasm and indelible mentorship.

## ACKNOWLEDGEMENT

I would first like to thank my supervisor, Dr. Chinthaka Mallikarachchi, for encouraging my interest in the biomimetic area, though relatively new to the department, and supporting me in every step of this work. His technical guidance, motivational words and patience have been invaluable in overcoming the hurdles along the way.

Next, I extend my sincere gratitude to Prof. Priyan Dias and Dr. Chathura Ranasinghe for the valuable comments and suggestions given during progress reviews. Their well-informed insights have never failed to be thought provoking. Also, I would like to take this opportunity to thank all the academic staff of the Department of Civil Engineering, University of Moratuwa, for laying a strong technical foundation.

Also, I thank my research colleagues Mierunalan, Chamith, Milinda, Hasitha and Sahangi for the numerous discussions at and outside group meetings, which have often led to opening new lines of thought in my present work.

Finally I would like to thank the National Research Council, Sri Lanka and Senate Research Committee of University of Moratuwa for the financial assistance provided.

# CONTENTS

# LIST OF FIGURES

## LIST OF TABLES



## LIST OF ABBREVIATIONS

| | |
|---|---|
| MAV | Micro Air Vehicle |
| UAV | Un-aided Air Vehicle |
| PIV | Particle Image Velocimetry |
| CFD | Computational Fluid Dynamics |
| CSD | Computational Structural Dynamics |
| FSI | Fluid Structure Interaction |

| | |
|---|---|
| LEV | Leading Edge Vortex |
| DOF | Degree of Freedom |
| FEM | Finite Element Method |
| FVM | Finite Volume Method |
| ALE | Arbitrary Lagrangian Eulerian4 |
| CSE | Co-simulation Engine |
| NSE | Navier Stokes Equation |
| VIV | Vortex Induced Vibrations |

## LIST OF APPENDICES

# CHAPTER I

## 1. BACKGROUND

### 1.1. Bio-inspired Deployable Structures

Micro Air Vehicles (MAVs) is a class of miniature unaided air vehicles (UAV) that have a size restriction of generally less than 15 cm. The Defence Advanced Research Projects Agency (DARPA), US, defines MAV as "an aircraft having a dimension lesser than 6 inches in any direction or a gross take-off weight lesser than 100 g". These are used for a wide variety of applications such as military surveillance, rescue operations in hazardous environment, crowd control, pollution inspection, urban traffic management, pipeline inspection, high risk indoor inspection and space exploration. Such applications require one or more of the following characteristics:

- Light weight
- Minimal power consumption
- Manoeuvrability
- Robust and durable structural framework

These factors are inter-related and rigorous design methods are required to ensure optimum performance. Weight is of major concern here, as it adds to the power

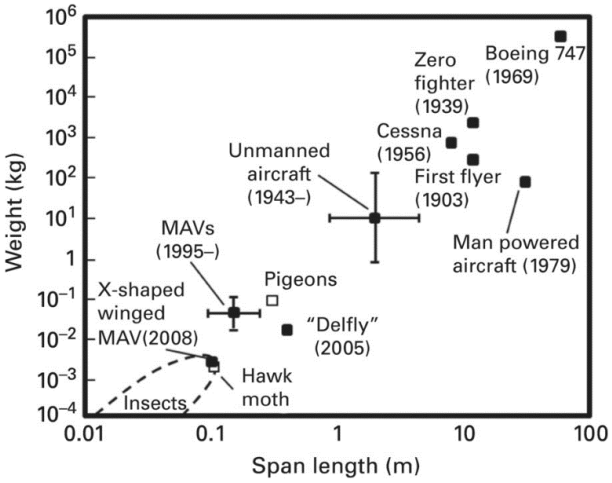


*Figure 1.1:* Weight to span relationship of different natural and man-made fliers. Source: (Taya, Van Volkenburgh, Mizunami, & Nomura, 2016)

requirement, leading to additional mass contributed by the power source as well. A general comparison of weight to span ratio of common fliers is given in Figure 1.1.

Depending on the size of the flying object, the aerodynamic principles exploited in flight differs. In order to gain understanding of these mechanisms researchers have turned to nature for inspiration and studied the miniature natural fliers, the insects. Some examples of such bio-inspired MAVs are shown in Figure 1.2.

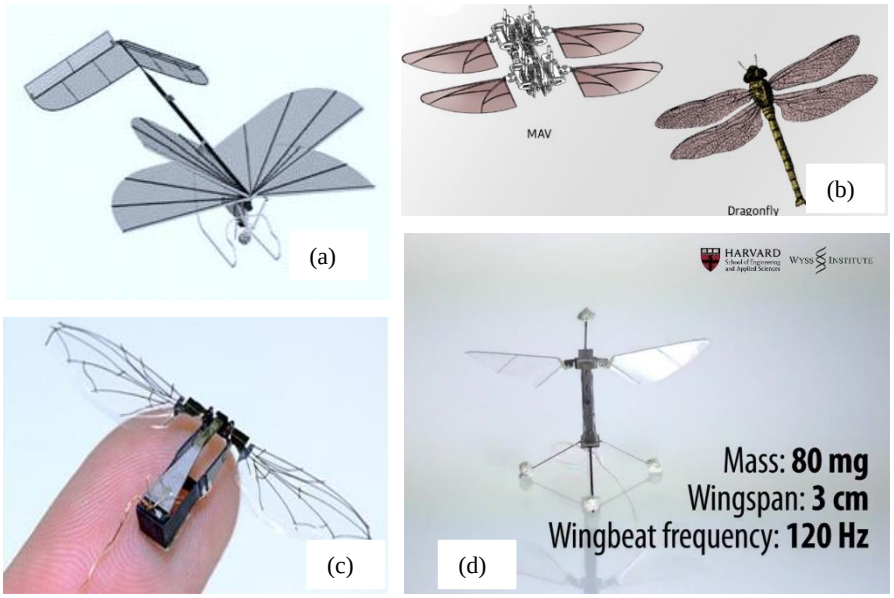


*Figure 1.2:* Bio-inspired MAVs with flapping flight mechanism (a) Delfly [TU Delft] (b) Multi-wing flapping MAV [Georgia Tech] (c) Microrobotic Fly [Harvard] (d) Robobee [Harvard]

However, the examples given in Figure 1.2 have a common feature, which is that the wings cannot be folded. It would be advantageous to have a deployable wing in an MAV so that a light-weight, membranous wing with a large surface area, that can generate sufficient lift force, can be safely folded back until it is required. In addition to protecting the wing, it will also provide the MAV with more manoeuvrability if it is to be designed for ground locomotion as well. But the deployment dynamics of the wing becomes complex when combined with the aerodynamic factors involved in this system. Again, nature provides examples of self-deployable wings, which not only perform the required folding and opening functions, but also achieve this in the most energy efficient way possible. Saito, Nomura,

Yamamoto, Niyama, & Okabe (2017), in a recent study on ladybird species *Coccinella septempunctata*, observed the deployment process in detail by removing two-thirds of the insect's elytra and replacing it with an artificial, transparent one. It was seen that the wing was folded back in an origami based pattern which facilitated smooth self-deployment, while the actual opening force was given by the snapping back of the veins. Here the veins act like deployable booms which are used in space applications. They use the energy stored during folding, to open back. Hence the requirement for additional actuators and power is avoided.

To replicate such a system, crease lines must be introduced in the membranous wing to localize the folding location, so that the wing folds back to the same configuration every time it is closed. Creases introduce a kink or a geometric distortion in an otherwise flat membrane. This aspect should be analysed in light of the effect it will have on the path of the air flowing around it during flight and thus the aerodynamic performance. Studies done on corrugations and flexion lines in insect wings (Wootton, 1979 and Combes, 2010) suggest that a change in the wing's cross sectional profile does have an effect on its resulting behaviour. The magnitude of the effect remains to be quantified.

### 1.2. Problem Statement

In order to study the effect of creases on the wing's performance, a suitable experimental or numerical setup should be devised. A number of experimental work has been done in this area (Zhao, Huang, Deng, & Sane, 2010).

However, manufacturing process of MAVs is tedious, especially as assembling should be done with precision despite working with parts of very small dimensions. The complex nature can be illustrated by Figure 1.3. Even simplified models can be hard to produce due to the intricacies involved in making just the wing, requiring special techniques like precise laser cutting and assembling under magnification. Also deployment would necessitate other techniques like self-opening of shape-memory alloys. These additional external factors will be cumbersome in determining a suitable crease pattern for folding the wing and each trial will be expensive and time consuming.

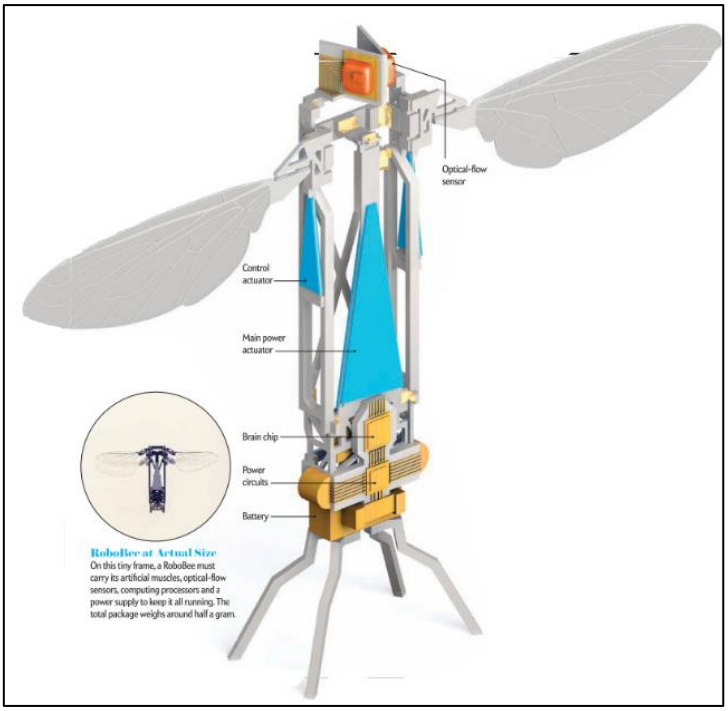


*Figure 1.3*: Robobee developed at Wyss Institute, Harvard. Source: (Wood, Nagpal, & Wei, 2013)

In addition to the structural aspect, a fluid domain set-up is required to study the aerodynamic parameters. Specialized techniques like Particle Image Velocimetry (PIV) are needed to monitor the flow pattern and wind or water tunnels with such capabilities are required for this study.

At testing phase, numerical models provide a relatively cost efficient means to test different parameters. For analysing the aerodynamic performance of a flexible wing, a FSI framework which can handle a highly deformable structure and the turbulence created by its movement is required. Usually this is dealt with by developing project specific in-house codes with such advanced capabilities. However, considering that the commercial codes available at present too have the flexibility to incorporate many advanced applications, the present work seeks to harness such features and unify it into an efficient numerical model.

## 1.3. Objective

The main objective of this study is to develop an efficient numerical model to study the fluid structure interactions involved in thin, membranous structures subjected to a steady flow of fluid using capabilities available in commercially available CSD and CFD codes. This will be achieved through the following individual sub-objectives.

- Identifying the appropriate commercial codes that can be used in an FSI analysis and their limitations
- Developing a coupled fluid-solid interaction framework and verifying against a standard benchmark

## 1.4. Outline

**Chapter 1** presents the background for conducting this study. This includes an introduction to deployable structures and biomimetic concepts in engineering applications. The need for a fluid structure interaction (FSI) framework and the objectives to be achieved in order to address it are also described.

**Chapter 2** gives an overview of the concepts related to insect-scale flight, description about the adaptations of an insect wing to facilitate flight and the related origami concepts. Also, the concepts related to FSI and the numerical techniques used so far are presented in detail. This chapter concludes with a comparison between two commercially available analysis environment ABAQUS and ANSYS and an in-depth study on the FSI capabilities of ABAQUS.

**Chapter 3** starts with a detailed study about the numerical implementation of structural, fluid and coupling modules. It goes on to describe the procedure followed to validate the proposed method.

**Chapter 4** discusses the outcomes of the FSI analysis. At first, an initially flat plate was analysed at two different inflow velocities and materials. Next, the analysis was extended to a membrane with a predefined crease geometry and the resulting flow was compared with the uncreased membrane's behaviour.

**Chapter 5** presents the findings of the research analysing the feasibility of the proposed method for FSI analysis of a thin flexible membrane.

**Chapter 6** discusses an overview on possible future improvements. A brief introduction to a crease modelling technique is reviewed.

# CHAPTER II

## 2. LITERATURE REVIEW

This chapter provides a brief overview of the theoretical concepts involved in FSI analysis and the work that has been conducted thus far in this area. Section 2.1 gives an introduction to the different principles governing the aerodynamic behaviour of structures of different length scale and the mechanisms employed by insects to achieve flight. Section 2.2 discusses the structure of an insect wing, paying attention to the material model and origami-based deployment mechanisms involved. In Section 2.3, a detailed review of the numerical simulation techniques is presented together with a software comparison made between the ABAQUS and ANSYS environments with regards to FSI analysis.

### 2.1. Insect-scale Flight Mechanisms

#### 2.1.1. Macro vs Micro Flight Mechanisms

Considering both biological and man-made flyers, it is evident that the principles governing their flight mechanisms is different based on factors such as their overall size. In an aeroplane, for example, the Bernoulli's principle is primarily employed to generate lift. Due to the shape of an aerofoil, the air flowing over it is at a higher velocity than that under it and the pressure difference thus generated causes an upward lift force. To achieve sufficient lift, the system has to move at high speed over some distance, as is the case with planes, which make use of a runway for this purpose and engine to provide the forward thrust. However, this is not feasible for all classes of flyers. Biological flyers such as birds and insects use the “flapping wing” and soaring mechanisms to overcome this limitation.

Flapping can be considered as a mode of powered flight. Force is produced by swinging the wing in an arc at the body-wing joint with stroke reversal happening at each half stroke. The direction and speed of flight is controlled by the tilt of the flapping stroke plane. Different biological flyers employ different flapping patterns resulting in various wing-tip paths as illustrated by Figure 2.1.

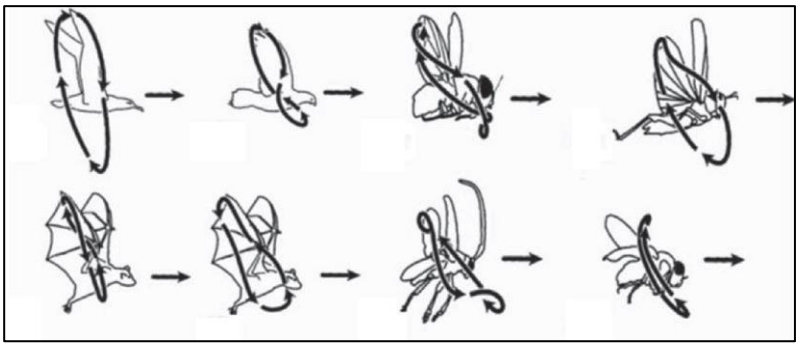

*Figure 2.1:* Wingtip paths relative to the body for a variety of flyers, as indicated by arrows. (a) albatross (b) pigeon (c) horseshoe bat (d) horseshoe bat (e) blow fly (f) locust (g) June Beetle (h) fruit fly. Source: Alexander (2004)

However, there is a major difference between bird and insect flight. Birds have active control over the flapping motion as they have a skeletal structure running through the wing, which allows them to have direct control over its shape even at intermediate locations. Insect wings, on the other hand, are attached to the body at only the wing base and the flapping motion is brought about by a set of flight muscles and other coupling structures present in their thorax, acting as a lever system (Wootton, 1981). This is given in Figure 2.2 which further shows the different setups involved in direct and indirect mechanisms. The motion thus produced is transferred throughout the wing via the vein framework.

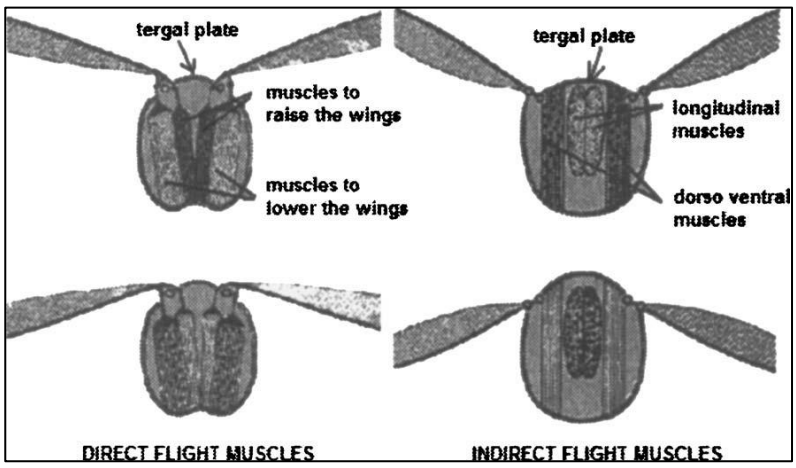


*Figure 2.2:* Flapping mechanisms in insects. Source: Madangopal, Khan, & Agrawal (2005) (Courtesy: Hooper Virtual Paleontological Museum)

### 2.1.2. Insect-scale Flight Concepts

Insects operate at low to midrange Reynolds numbers of order $10^1$ to $10^4$ (Hao Liu, 2009). Owing to this they are referred to as "low Reynolds number fliers". MAVs designed at insect scale were originally envisioned to achieve Reynolds numbers of order $10^4$ to $10^5$ due to the inherent issues related to such a type of flight. However, as the understanding of the underlying concepts improved, it has been possible to achieve lower numbers (Shyy, Lian, Tang, Viieru, & Liu, 2007).

The aerodynamic concepts governing flight at insect-scale is different from that at a macro level. The main lift production mechanism is through vortices that circulate bound to the wing surface, creating a pressure difference between the upper and lower sides of the wing (R. Wootton, 1999). It has been observed that the lift produced by a flapping wing mechanism is higher than that derived from conventional aerodynamic calculations. To account for this discrepancy specialized "high-lift" mechanisms, such as the production of a Leading-Edge Vortex (LEV), were postulated (Ellington, Van Berg, Willmott, & Thomas, 1996). The authors. have confirmed this theory through experimental observations made on a hawk-moth.

LEV is formed when the wing is suddenly accelerated at a high angle of attack. This occurs just near the wing's leading edge, so that the flow, which separates on passing around the aerofoil profile, reattaches again to the surface. This phenomena by itself is very short lived. However, the flapping motion has been observed to stabilize this (Haas & Wootton, 1996). Thus the LEV gradually moves in a swivelling path attached to the wing, producing a high velocity and low pressure zone at the core of its path as shown in Figure 2.3.

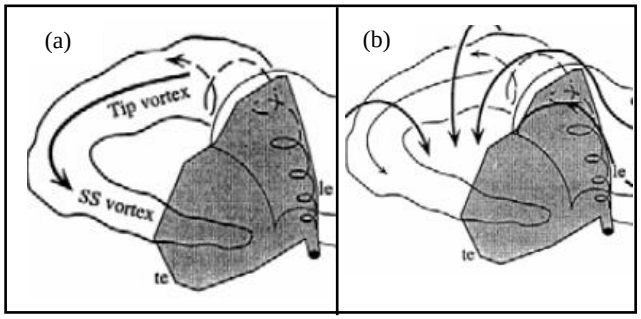


*Figure 2.3:* (a) Path of the vortex on the upper surface of the wing (b) Suction zone created at the core of the vortex. Source: Viieru, Tang, Lian, Liu, & Shyy (2006)

## 2.2. Wing Structure of Insects

### 2.2.1. Material Model

Insect wings are basically very thin, membranous structures which are held in place by a stiffer framework made up of the veins. Due to the large deformations involved, a typical Hookean model cannot be used to describe their behaviour. Ideally, a Mooney-Rivlin or Neo-hookean hyperelastic model should be adopted instead (Jenkins, 1996).

Considering the Green Deformation Tensor, C, of the material, its invariants $I_1^C$, $I_2^C$ *and* $I_3^C$ can be given as in Equation 2.1.

$$\begin{aligned} I_1^C &:= \mathrm{tr}(\mathbf{C}) = C_{II} = \lambda_1^2 + \lambda_2^2 + \lambda_3^2 \\ I_2^C &:= \tfrac{1}{2}\left[(\mathrm{tr}\ \mathbf{C})^2 - \mathrm{tr}(\mathbf{C}^2)\right] = \tfrac{1}{2}\left[(C_{JJ})^2 - C_{IK}C_{KI}\right] = \lambda_1^2\lambda_2^2 + \lambda_2^2\lambda_3^2 + \lambda_3^2\lambda_1^2 \\ I_3^C &:= \det(\mathbf{C}) = \lambda_1^2\lambda_2^2\lambda_3^2. \end{aligned} \tag{2.1}$$

Here, $\lambda_i$ denotes the principal stretch in the i-direction. For incompressible material the third invariant is obviously 1, i.e. $\lambda_1\lambda_2\lambda_3=1$. Mooney (1940) exploited this relationship in simplifying the complex strain energy function by considering the deformation in two steps: first, being a stretch and squeeze; the second, a shear deformation in the plane normal to the stretch. In his work, starting from the relationship in Equation 2.2 a simpler linearized function to describe the strain energy, W, was obtained as in Equation 2.3.

$$W = W(I_1, I_2, I_3) \tag{2.2}$$

$$W = c_1(I_1 - 3) + c_2(I_2 - 3) \tag{2.3}$$

where $c_1$ and $c_2$ are material constants. This relationship appropriately describes the behaviour of naturally occurring hyper-elastic material such as the one at hand. The material parameters should be determined using uniaxial or biaxial testing procedures (Selvadurai & Shi, 2012).

### 2.2.2. Deployable Wings

In human limbs and bird wings, the presence of a bone-muscle framework makes folding and unfolding, a repeatable, actively controlled mechanism. In insect wings such a system is not present and thus calls for a different mechanism (Wootton, 1981).

Initially two different basic mechanisms were postulated: one states that the original position of the wing is the fully deployed state, and it is folded back with the help of the hind legs or the abdomen; other states that the natural position of the wing is in folded configuration and it is unfolded and kept rigid through the vein framework (Forbes, 1924). Later entomological works like Wootton (1979), Brackenbury (1994) and Haas and Wootton (1996), have presented detailed studies confirming the presence of a retraceable folding configuration which also facilitates the opening process. Recent observations made by Saito, et al. (2017) on a ladybird by replacing its elytron with a transparent, artificial one and recording through a high speed camera (Phantom V1611), further verify this theory. Also, the authors, in an earlier work, have presented a "elastic origami model" to describe the deployment process (Saito, Tsukahara, & Okabe, 2015), which will be discussed in more detail in Section 2.2.3.

Similarly, Deiters, Kowalczyk, & Seidl (2016) have pointed out through literature and personal records that folding ratios of 1:10 and 1:18 have been observed in *Forficula auricularia* and *Labia minor* earwig species. This was achieved through a fan-like folding process. The stability of the unfolded wing was studied and it was identified that this was ensured through in-built mechanisms in the wing such as the "mid-wing mechanism" discussed in Section 2.2.3**.**

### 2.2.3. Origami Concepts

A crease can be considered as a geometric non-linearity introduced in a surface which is initially flat relative to the final configuration. The fold-lines are classified into convex (mountain fold) or concave (valley fold) as shown in Figure 2.4.

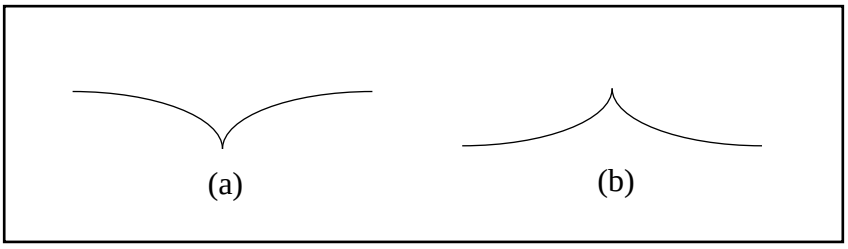


*Figure 2.4:* (a) valley fold (b) mountain fold

A flat plate with a single fold-line can be considered as an assembly of two rigid panels connected at the fold-line by a hinge. The simplified "rigid folding" model

based on the above consideration assumes that the panels remain flat while the entire creasing deformation is concentrated at the fold-line (Lebée, 2015).

The combination of two or more such crease lines results in folding mechanisms that form the basis of the ancient art of folding, known as “Origami”. A sample folding pattern is given in Figure 2.5.

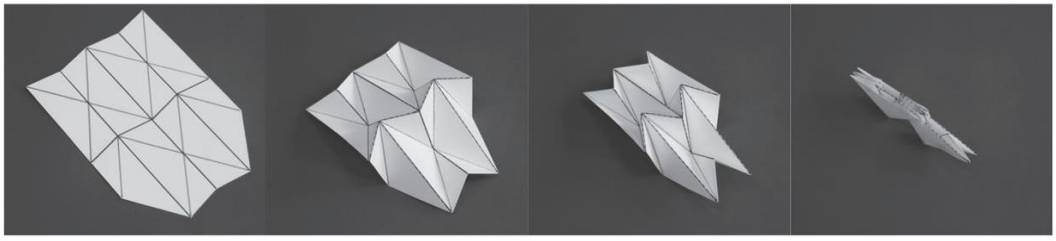

*Figure 2.5:* Folding sequence of thin membranes with “waterbomb” origami pattern
Source: Chen, Feng, Ma, Peng, & You (2016)

Similar concepts have been observed in deployable structures in nature. Leaves of certain plants like the hornbeam exhibit this property (Mahadevan, 2005). Another good example, which is also the application of primary concern in this study, is the deployable wings of some insects like the ladybird. Saito et al. (2017) investigated the folding and deployment mechanism of the *Coccinella septempunctata* species and confirmed the exploitation of origami concepts in the process.

The shape morphing technique in the wing can be simplified into a mechanism consisting of four creases meeting at common intersection point, known as the knot. This is shown in Figure 2.6. Also it gives the different combination of mountain and valley folds such that different folded configurations can be achieved. The opening and closing processes are controlled by changing the angle ε as illustrated by Figure 2.7. The semi-transparent wing captured by Saito et al. (2017) clearly shows how this mechanism is incorporated in the wing structure (Figure 2.8).

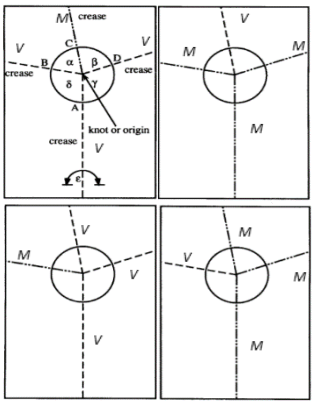


M – Mountain fold

V – Valley Fold

*Figure 2.6:* Simplified representation of the folding mechanism of an insect wing Source: Haas & Wootton (1996)

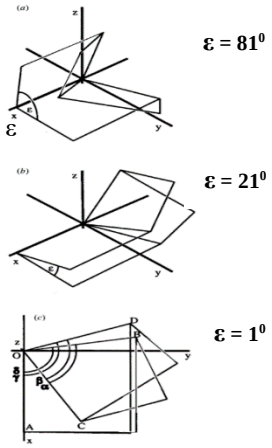


*Figure 2.7:* Different combinations of M and V folds forming the insect wing folding mechanism. Source: Haas & Wootton (1996)

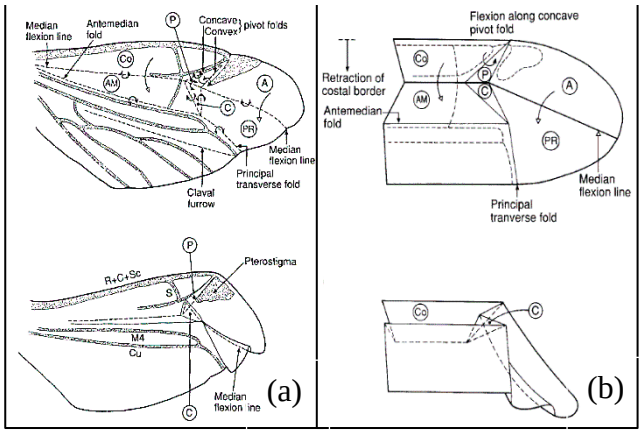


*Figure 2.8:* (a) Folding mechanism in insect wing (b) Schematic representation Source: Brackenbury (1994)

Brackenbury (1994) has studied similar mechanisms in other insect species. The comparison is given in Figure 2.9. The main role played by the concave, median flexion line and the convex, principal transverse fold in the folding process are clearly seen in this illustration.

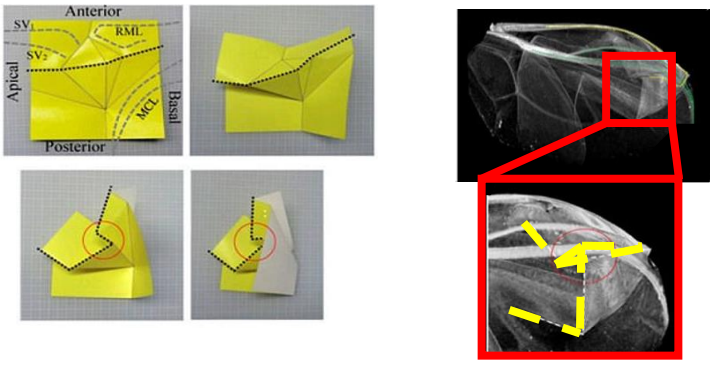


*Figure 2.9:* (a) Paper model of the diamond-shaped crease pattern seen in the hind wings of ladybirds (b) Origami folding pattern in ladybird hind wings Source: Saito et al. (2017)

This mechanism can be explained using the "Elastic Origami" model proposed by Saito et al. (2015). The creased surface is represented as a three dimensional truss with truss elements and pin joints replacing the fold-lines and vertexes and additional members along the diagonal of the facets as shown in Figure 2.10. Saito et al. have point out that, apart from special cases like the Miura-ori pattern, other patterns which can be represented as a stable truss structure (i.e. degree of freedom $\leq 0$) cannot be folded. However, if one element is replaced by an elastic member, this stability is disturbed. The structure can either be in open or closed configuration and the deployment process can be entirely controlled by the elastic member. This mechanism is illustrated in Figure 2.11.

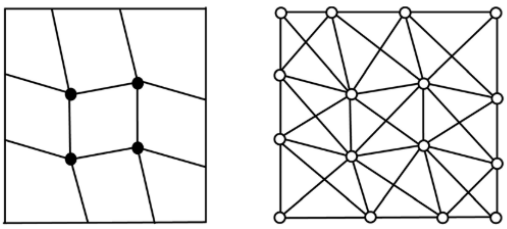

(a) (b)

*Figure 2.10:* (a) Creased surface (b) 3-D truss representation of surface in (a)

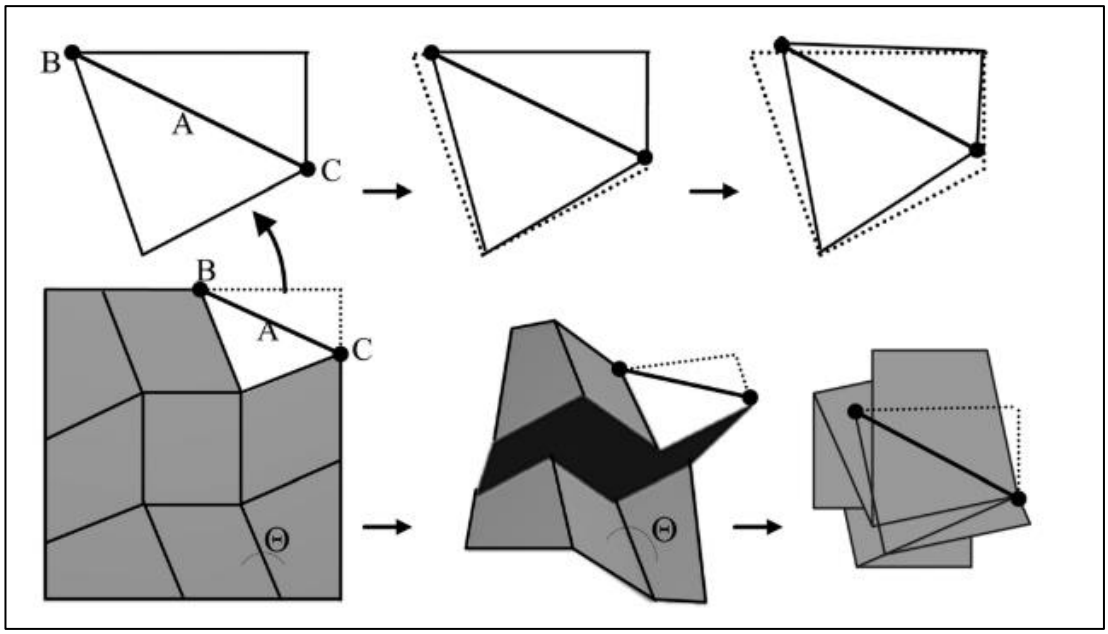


*Figure 2.11:* Partially elastic origami model. The elastic beam A deforms progressively throughout the folding process, enabling the stucture to collapse into the final closed configuration. Source: Saito et al. (2015)

## 2.3. Numerical Simulation techniques

### 2.3.1. Basic Concepts related to FSI Simulation

The complexity of an FSI problem can be decided based on the nature of the structural response as shown in Figure 2.10. In this figure, it can be clearly seen that the complexity level increases from left to right.

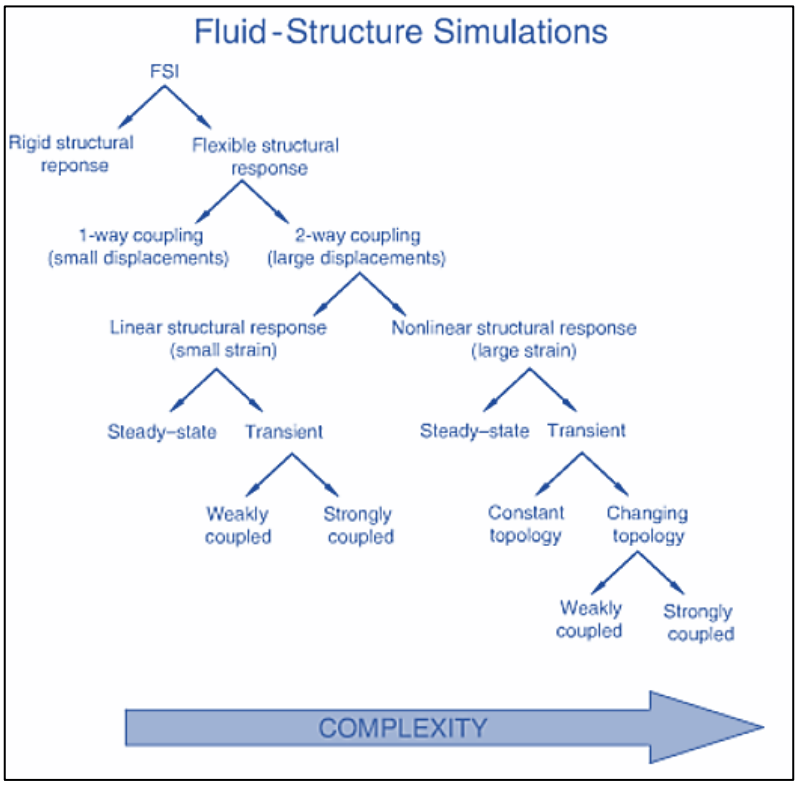


*Figure 2.12*: Complexity level of an FSI analysis
Source: ABAQUS Analysis User's Manual

Depending on this extent of complexity one of the following analysis approaches can be chosen:

- **6-DOF Solver**: This is suitable for rigid body structural response
- **Simple FSI** : The structure is assumed to deform linearly and the eigenmodes are considered sufficient to describe the structural response. Thus, the coupling effect is incorporated via compliance matrices.

- **Staggered/ Partioned Approach** :
  The structural and fluid responses are calculated separately and exchanged at the interface at certain intervals.
- **Specialized techniques** :
  e.g. Smooth-particle hydrodynamics (SPH)
- **Monolithic Approach** :
  Both fluid and structural responses are incorporated in the same equation and solved together.

The staggered approach has the advantage that it is less time consuming, memory allocation required is less and it is easily implemented using available commercial codes.

### 2.3.2. State of the Art in FSI Analysis

The issues associated with modelling the aerodynamic response of insect wings are mainly due to its thin, membranous nature, which makes it highly deformable and the unsteady aerodynamic flow associated with insect-scale flight. In addition, the mass and thickness of the actual wing is not uniform throughout, leading to complex structural FSI response.

In initial works, models have been developed under the assumption that the insect wings act as rigid plates (Smith, Wilkin, Williams, & Lafayette, 1996). However, later studies have identified the significance of wing flexibility in the resulting wing performance. Mountcastle & Combes (2013) performed a study by stiffening the wings of bumblebees. They found that these specimens showed a reduction of 8.6% in the lift production compared to the natural fliers. Thus, it follows that a numerical model which does not capture the wing flexibility would under-predict its performance. This is especially significant due to the very low thickness of these membranous structures. The thickness is generally in the order of micrometers. For example, that of *Allomyrina dichotoma* beetle wings is 4.5 μm in average (Ha, Truong, Goo, & Park, 2013), while dragon flies are shown to exhibit a variation between 3.6 μm to 15 μm (Jongerius & Lentink, 2010).

To incorporate the wing flexibility and the associated wing camber, membrane models were developed. Initially these were developed based on the "Sail Equation" (Newman, 1987) given by Equation 2.4.

$$1 - \frac{C_T}{2} \int_0^1 \frac{\frac{d^2(y/a)}{dx_1^2}}{2\pi(x_1 - x)} dx_1 = \frac{d(y/a)}{dx} \tag{2.4}$$

where the profile of the cambered membrane is given as a function of x coordinate, incidence angle (α) and tension coefficient ($C_T$). However this relationship itself is valid only for inextensible membranes in steady, inviscid flow fields. To extend such models to bio-membranes, the membrane mechanics relationships have been considered together with hyper-elastic of visco-elastic material models (Lian, Shyy, Ifju, & Verron, 2002).

Issues associated with numerical simulation of membranous structures having non-unique load paths and associated FSI analysis have been of interest for a long time. Extensive work has been done prior to the 1990s as summarized by Jenkins & Leonard (1991). FEM techniques have since been developed to handle structural response involving large deformations. However, pneumatic membranes with underconstrained degrees of freedom have posed a hurdle in this development history. The stiffness provided by the material takes effect only under certain loaded conditions and the behaviour is often non-unique until such a configuration is reached (Jenkins, 1996). Also, the possibility of wrinkling, due to the inability of thin membranes to bear compressive loads, adds further complexity to the analysis. The tension field theory was developed, as a result of the works of Wagner in 1929 and Reissner in 1938, to address such issues. However, models developed on similar grounds provided a basis to study the stress distribution at regions where wrinkling occur, but not the salient features characterising the actual wrinkled geometry. FEM models have the disadvantage of not being able to attain a straight forward convergent solution. This has been overcome by methods such as introducing pseudorandom imperfections in the membrane geometry to induce buckling (Tessler, Sleight, & Wang, 2003). At the same time, wave based models have been developed and shown to have more

agreement with experiments than FEM when solved with simplifications specific to different geometric shapes (Liu, Huang, & Wang, 2017).

The selection of appropriate model and parameters for the fluid domain too is a key in FSI analysis of insect wings. As with any fluid dynamics problem, the basic Navier-Stokes equation should be satisfied, i,e, mass, momentum and energy balance should be implemented. In addition the turbulence near the moving boundary region even at a low Reynolds number should be captured. Spalart-Allmaras turbulence model was shown to be suitable for this application by Thill, Downsborough, Lai, Bond, & Jones (2010). However, the authors point out that the applicability for the region where flow separation takes place should be verified.

The fluid domain mesh is another aspect of concern as it has to handle the embedded moving boundary. Arbitrary Lagrangian Eularian (ALE) mesh has been used in a number of works, as this gives a relatively smooth mesh deformation as the solution proceeds. This method is discussed in detail in Section 2.3.4 (A). Immersed boundary layer method (IBM) is another method that is widely used in FSI problems, especially in biomechanical and biomedical applications (Tian, Dai, Luo, Doyle, & Rousseau, 2014). It was originally introduced by Peskin (1972) for the purpose of studying the heart valve. In this method the boundary is considered as part of the fluid and the structural domain is replaced and monitored in terms of an Eularian mesh (Rowlatt & Phillips, 2016). Tian, Dai, Luo, Doyle, & Rousseau (2014) developed an in-house FORTRAN code based on the IBM and coupled using an implicit scheme.

Monolithic FSI approach and strongly coupled partitioned approach generally require in-house codes. In the works by De Nayer, Kalmbach, Breuer, Sicklinger, & Wüchne (2014) and Tian et al. (2014), rigorous numerical codes were developed and tested for the case of a flow around a cylinder with a flexible flap attached to the downstream side. Nguyen, Shyam Sundar, Yeo, & Lim (2016) have developed a similar scheme specifically for studying insect-scale wings and have presented it together with a set of verification tests used along the way to test the proposed method.

### 2.3.3. ABAQUS vs ANSYS Workbench

The ABAQUS environment, created by Dassault Systems Inc., offers structural and CFD modules which can be used in an FSI Analysis. Both Implicit and Explicit solvers are available for this purpose. The structural solver uses Finite Element Method (FEM) while the CFD module uses a hybrid formulation which combines both FEM and FVM (Finite Volume Method). Being initially designed to address non-linear material and contact-related response and handling linear problems as a special case of it, ABAQUS provides a robust framework for a wide range of structural applications. ABAQUS/CFD is an incompressible, pressure-based solver. It provides the capabilities to incorporate buoyancy driven flow and use energy equation for thermal analysis. Also turbulence models such as Spalart-Allmaras and K-ε model are available. Arbitrary Lagrangian Eulerian (ALE) meshing capability is available for applications involving deforming mesh and moving boundaries.

For FSI data exchange, ABAQUS provides coupling between ABAQUS/Standard and ABAQUS/Explicit with ABAQUS/CFD or external codes. The former is achieved through the Co-simulation Engine (CSE) while the latter (i.e. coupling between an ABAQUS solver and an external solver) can be done using an external coupling code. Currently, MpCCI (Multi-Physics Code Coupling Interface) from Fraunhofer SCAI is compatible with ABAQUS and many other commercially available CSD and CFD codes.

ANSYS provides an integrated Workbench environment that acts as a common platform for connecting different solvers such as Fluent, which are optimised for specific applications. These solvers are available as individual modules in the Workbench interface and can be added to the project together with other tools such as “coupling” module. This makes ANSYS Workbench more user-friendly towards multi-physics applications. In addition, this provides a very efficient meshing tool which is especially important in CFD analysis in achieving refined mesh in the boundary layer region.

### 2.3.4. FSI Analysis Capabilities in ABAQUS

#### A. Arbitrary Lagrangian Eulerian (ALE) Mesh

A Langrangian description of a fluid flow refers to the observation made by an observer moving with the fluid. In other words, it tracks the path of a single fluid particle over time and space. In contrast, the Eulerian description can be made in terms of the observations made by an observer fixed at one position, i.e. the position of fluid particles moving through the point under observation is recorded over time. Similarly, in a numerical implementation, the Lagrangian mesh deforms with the moving material, while the Eulerian mesh remains fixed in one position and assesses the material moving through it at specified time increments. The former is used in most structural analysis, while CFD mesh is primarily Eulerian in nature.

In an FSI analysis, a moving boundary is involved. If an Eulerian mesh is used in the fluid domain it would require heavy refinement to capture the details near this boundary. A Lagrangian mesh on the other hand will undergo severe distortion if applied directly or would require many number of remeshing iterations in the course of the analysis to preserve the mesh quality. In earlier works this has posed a serious hurdle and complex grid rotation and application-specific adaptive techniques were used as in Liu and Kawachi (1998).

A solution to this is presented in the form of ALE mesh, which combines the functionalities of both types discussed above. In this, typically a Lagrangian time step is followed by an advection step in which the distorted Lagrangian mesh is updated to a new undistorted mesh. In an Eulerian mesh, solution is mapped back onto the original mesh. But in ALE, solution is mapped into a newly updated mesh. Thus, ALE avoids the need for remeshing and high mesh density. Figure 2.13 presents a schematic conceptual description of all three methods and Figure 2.14 gives a comparison of the capabilities of ALE in contrast to the Lagrangian description in accommodating excessive distortion.

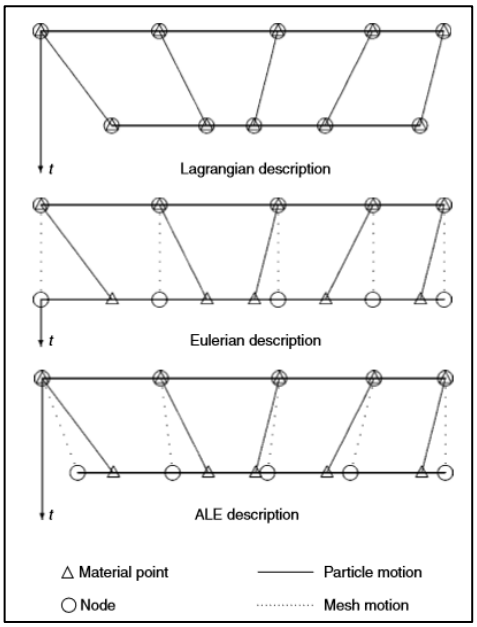


*Figure 2.13:* Conceptual description of Lagrangian, Eulerian and ALE mesh

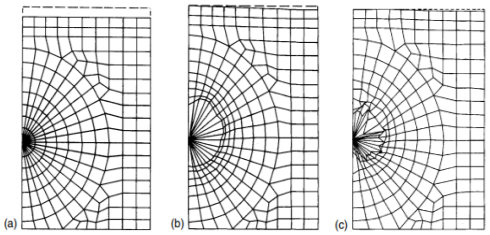


*Figure 2.14:* (a) Initial mesh (b) Distorted ALE mesh (c) Lagrangian
Source: Donea, Huerta, Ponthot, & Rodríguez-Ferran (2004)

The ALE formulation is based on the relative velocities between material and mesh as given by Equation 2.5. The main solution procedure is implemented at the fluid-structure interface and boundaries and interpolated elsewhere. A quantity of interest *f* such as displacement, originally in the coordinate system x, is mapped to ALE coordinates *X* using the relative velocity *w*.

$$\frac{\partial f(X_i,t)}{\partial t} = \frac{\partial f(x_i,t)}{\partial t} + w_i \frac{\partial f(x_i,t)}{\partial x_i} \tag{2.5}$$

## B. Solution Controls

Abaqus provides solution control for non-linear solutions and time incrementation in the Abaqus/Standard product and FSI stabilization controls for co-simulation between Abaqus/CFD and Standard or Explicit solver (Abaqus, 2014).

Abaqus treats the moving mesh domain in the FSI analysis as a pseudo-elastic problem. Computational time can be reduced by reducing the number of smoothing iterations or relaxing the linear convergence criteria. Increasing these parameters ensures good mesh quality.

A “Penalty scale factor” is available in Abaqus to impose stabilization of the FSI solution. It has a default value of 1, but can be increased to accommodate extremely flexible structures. Increasing this value in increments of 0.1 is recommended by the manual (Abaqus, 2014).

# CHAPTER III

## 3. FSI SIMULATION OF THIN FLEXIBLE STRUCTURES

This chapter presents a detailed description of the theoretical concepts used in developing the FSI framework of a flexible structure immersed in fluid. Section 3.1 presents the numerical formulation behind the procedures followed to set-up the structural and fluid domains and the coupling algorithm. Section 3.2 gives the verification for fluid domain and the overall numerical FSI framework.

### 3.1. Numerical Implementation Concepts

A detailed review of the underlying principles in the numerical implementation of computational structural dynamics (CSD) and computational fluid dynamics (CFD) is presented in this chapter. The CSD code is based on the Finite Element Method (FEM), while CFD is based on a hybrid of FEM and FVM (Finite Volume Method). The coupling scheme involves an explicit Gauss-Seidel algorithm.

#### 3.1.1. Structural Domain

The CSD formulation can be derived based on the virtual work theory. Let the displacement u in the three dimensional space be given by Equation 3.1.

$$u(X,Y,Z) = \sum_k h_k(X,Y,Z)u_k = [H]\{u\} \quad (3.1)$$

where $h_k$ and $u_k$ are the shape function and displacement respectively of the $k^{th}$ node in the considered element and can be written in matrix form as given in the second part of the equation, where [H] is a matrix containing $h_k$ and {u} is the vector containing $u_k$. Based on the balance of internal and external forces acting on a dynamic structural system, the following general relationship can be obtained:

| Inertial Force | + Damping Force | + Internal body-stress Forces | = Externally Applied Load |
|---|---|---|---|

Using principle of virtual work, the above relationship can be written for the equilibrium of an element as given by Equation 3.2.

$$[M]\{\ddot{u}\} + [C]\{\dot{u}\} + \{F\} = \{P\} \tag{3.2}$$

where [M] is the mass matrix, [C] is the damping coefficient matrix, {F} is the force vector containing internal body stresses and {P} is the external force vector. Tian et al. (2014) have presented a comprehensive FEM formulation for each of the above terms. This is given in Equations 3.3 to 3.6.

$$[M] = \sum_m \int_{V_m^0} \rho_s [H]^T [H] dV \tag{3.3}$$

$$[C] = \sum_m \int_{V_m^0} \eta_d [H]^T [H] dV \tag{3.4}$$

$$\{\mathrm{F}\} = \sum_{\mathrm{m}} \int_{\mathrm{V_m^0}} [\mathrm{B_E}]^{\mathrm{T}} [\sigma^{\mathrm{K}}] \mathrm{dV} \tag{3.5}$$

$$\{\mathrm{P}\} = \sum_{\mathrm{m}} \int_{\mathrm{V_m^0}} \rho_{\mathrm{s}} [\mathrm{H}]^{\mathrm{T}} \{\mathrm{b}\} \mathrm{dV} + \sum_{\mathrm{m}} \int_{\mathrm{A_m^0}} [\mathrm{H}]^{\mathrm{T}} \{\mathrm{F}\} \mathrm{dA} \tag{3.6}$$

where $[B_E]$ contains the strain tensor $E_{ij}$ with respect to the displacement and {P} is given as a summation of body forces and surface forces. The components are integrated over volume or area as is relevant with $V_m^0$ and $A_m^0$ being the initial volume and area respectively.

Here the internal stress force can be modelled as a spring-mass system. Based on that the incremental component of the internal body stresses can be written as in Equation 3.7

$$\{\delta F\} = [K_T]\{\delta u\} \tag{3.7}$$

where $[K_T]$ is the total stiffness matrix, which is derived based on the material model being used. For an elastic material, the governing stress-strain relationship would be of the form given by Equation 3.8.

$$\sigma_{ij}^K = D_{ijm} E_{mn} \tag{3.8}$$

Here, $\sigma_{ij}^K$ is the second Piola-Kirchhoff stress tensor related to the Lagrangian strain through elastic matrix component $D_{ijm}$. Similarly, in the case of a Mooney-Rivlin hyper-elastic material, the stress-strain relationship can be derived based on the strain energy W given by Equations 3.9.

$$W = c_1(I_1 - 3) + c_2(I_2 - 3) \quad (3.9)$$

where, $I_1$ and $I_2$ refers to the invariants of the non-trivial solution for the strain relationship discussed in Section 2.2.1. and $c_1$ and $c_2$ are material constants which should be determined using uniaxial or biaxial testing procedures (Selvadurai & Shi, 2012).

### 3.1.2. Fluid Domain

A hybrid FEM-FVM (Finite Element and Finite Volume Method) formulation is used in Abaqus. In this approach, pressure calculation is based on a node-centred FEM and other transport variables such as velocity, temperature and turbulence are based on cell-centred FVM. The Projection Method is adopted in this work to solve the Navier-Stokes Equation (NSE). According to this, the pressure term and other variables are de-coupled and solved successively in two steps as explained below.

STEP 1:- Pressure term in NSE is ignored & intermediate velocity is calculated using a time discretization scheme

Temporal schemes available: Backward Euler, Galerkin, Trapezoid (Crank-Nicolson)

STEP 2:- Intermediate velocity is then corrected for pressure term

In the current work backward Euler time discretization scheme was chosen. It is an implicit scheme that is more appropriate for steady state solutions. An explicit scheme is more suitable for the present work, but this requires the use of very small time steps to obtain physically meaningful results (i.e. to prevent the wave from propagating to more than one cell in one time-step as difference equations typically involve only neighbouring cells and those beyond have no numerically defined influence on the solution of the cell under consideration). In the implicit method, numerical damping is applied making the solution stable even at relatively larger time steps, but this also makes the solution inaccurate in assessing the intermediate transient response. However, a computationally less expensive method was required for the initial assessment of the current system and thus the implicit scheme was chosen.

For a first order ordinary differential equation system of the form given in Equation 3.10, the standard time discretization scheme can be written as Equation 3.11.

$$\begin{cases} \frac{du}{dt} + R(u,t) = 0\,, & for\ t \in (t^n, t^{n+1}) \\ u(t^n) = u^n\ , & \forall n = 0,1,\ldots..,M-1 \end{cases} \tag{3.10}$$

$$\frac{u^{n+1} - u^n}{\Delta t} + [\theta R(u^{n+1}, t^{n+1}) + (1-\theta)R(u^n, t^n)] = 0, \qquad 0 \le \theta \le 1 \tag{3.11}$$

Here, θ is the measure of implicitness and takes a value between 0 and 1 according to the method being used. In backward-Euler method, θ=1, which makes it a fully implicit scheme. This has been adopted for the current work.

Applying this time discretization in combination with the Projection Method, the momentum conservation equation is obtained in the form shown in Equation 3.13. An intermediate velocity $u_i^*$ is introduced to this same relationship for the de-coupling purpose and taking the divergence this yields Equation 3.13.

$$\frac{u_i^{n+1} - u_i^n}{\Delta t} + \frac{\partial u_j^{n+1} u_i^{n+1}}{\partial x_j} = \frac{\partial}{\partial x_j}\left(\mu \frac{\partial u_i^{n+1}}{\partial x_j}\right) - \frac{1}{\rho}\frac{\partial p^{n+1}}{\partial x_i} \tag{3.12}$$

$$\frac{1}{\Delta t}\frac{\delta u_i^*}{\delta x_i} + \frac{\partial}{\partial x_i}\left(\frac{\partial u_j^m u_i^m}{\partial x_j}\right) = \frac{\partial}{\partial x_i}\left(\frac{\partial}{\partial x_j}\left(\mu \frac{\partial u_i^m}{\partial x_j}\right)\right) - \frac{\partial}{\partial x_i}\left(\frac{1}{\rho}\frac{\partial p^{n+1}}{\partial x_i} - \frac{1}{\rho}\frac{\partial p^*}{\partial x_i}\right) \tag{3.13}$$

Since the actual quantities involved are only those enclosed by the dashed lines in Equation 3.13, the relationship in Equation 3.14 naturally holds.

$$\frac{\partial}{\partial x_i}\left(\frac{1}{\rho}\frac{\partial p^*}{\partial x_i}\right) = \frac{1}{\Delta t}\frac{\delta u_i^*}{\delta x_i} \tag{3.14}$$

This is then used in the correction term as given in Equation 3.15.

$$\frac{u_i^{n+1} - u_i^*}{\Delta t} = -\frac{1}{\rho}\frac{\partial p^*}{\partial x_i} \tag{3.15}$$

In addition, the turbulence model too was incorporated in the current work in order to capture the vortex production. . The Spalart-Allmaras model, given by Equation 3.16, was chosen for this purpose and was used to calculate the kinematic viscosity $\hat{v}$.

$$\frac{\partial \hat{v}}{\partial t} + \mathrm{v}.\nabla\hat{v} = \underbrace{\frac{1}{\sigma}\left(\nabla\left((\hat{v}+v)\nabla\hat{v}\right) + c_{b2}|\nabla\hat{v}|^2\right)}_{\text{Diffusion}} + \underbrace{c_{b1}\hat{S}(\hat{v})\hat{v}}_{\text{Production}} - \underbrace{c_{w1}f_w(\hat{v})\left(\frac{\hat{v}}{d}\right)^2}_{\text{Dissipation}} \tag{3.16}$$

where the damping functions and the model coefficients are as follows (ABAQUS 6.14 Documentation, 2014)

$$f_w = g\left(\frac{1+c_{w3}^6}{g^6+c_{w3}^6}\right)^{\frac{1}{6}} \qquad g = r + c_{w2}(r^6 - r),$$

$$f_{v1} = \frac{\chi^3}{\chi^3 + c_{v1}^3}, \qquad r = \frac{\widetilde{\nu}}{\widetilde{S}\kappa^2 d^2},$$

$$f_{v2} = 1 - \frac{\chi}{1+\chi f_{v1}}, \qquad \widetilde{S} = S + \frac{\widetilde{\nu}}{\kappa^2 d^2} f_{v2},$$

$$\chi = \frac{\widetilde{\nu}}{\nu}, \qquad S = \sqrt{2R_{ij}R_{ij}},$$

$$R_{ij} = \frac{1}{2}\left(\frac{\partial u_i}{\partial x_j} - \frac{\partial u_j}{\partial x_i}\right)$$

Table 3.1: Spalart-Allmaras model coefficients

| $c_{b1}$ | $c_{b2}$ | $c_{v1}$ | $\sigma$ | $c_{w1}$ | $c_{w2}$ | $c_{w3}$ | $\kappa$ | $c_{v2}$ |
|---|---|---|---|---|---|---|---|---|
| 0.1355 | 0.622 | 7.1 | 0.6667 | $\frac{c_{b1}}{K^2} + \frac{1+c_{b2}}{\sigma}$ | 0.3 | 2 | 0.41 | 5 |

Abaqus uses a hybrid wall function implementation. For fine mesh, a wall-function free approach is implemented using a single smooth correlation proposed by Reichardt (1951). For coarse mesh, a near-wall gradient, which asymptotes to conventional solution, is achieved using an effective edge viscosity concept.

### 3.1.3. Mesh

Lagrangian mesh is used for the structural domain, while Arbitrary Lagrangian–Eulerian (ALE) is used for the fluid domain for the purpose of incorporating the movements of an immersed, flexible structure.

The ALE formulation used is similar to that discussed by Angel Fernández and Fernández (2011). Consider an ALE mapped domain $A_t$ belonging to the fluid domain $\Omega_f(t)$. The NSE written in this context is given by Equation 3.17.

$$\begin{cases} \rho^{\mathrm{f}} \partial_t \boldsymbol{u}|_{\boldsymbol{\mathcal{A}}} + \rho^{\mathrm{f}} (\boldsymbol{u} - \boldsymbol{w}) \cdot \boldsymbol{\nabla} \boldsymbol{u} - \mathbf{div}\, \boldsymbol{\sigma}(\boldsymbol{u}, p) = \mathbf{0} \quad \text{in} \quad \Omega^{\mathrm{f}}(t), \\ \qquad\qquad\qquad\qquad \operatorname{div} \boldsymbol{u} = 0 \quad \text{in} \quad \Omega^{\mathrm{f}}(t), \end{cases} \tag{3.17}$$

Here, $\rho^f$ is the density of the fluid, $\partial_t u|_A$ is the ALE time derivative, $\sigma$ (u, p) is the fluid Cauchy stress tensor and $\mu$ the fluid dynamic viscosity. This is implemented together with the boundary conditions indicated in Figure 3.1.

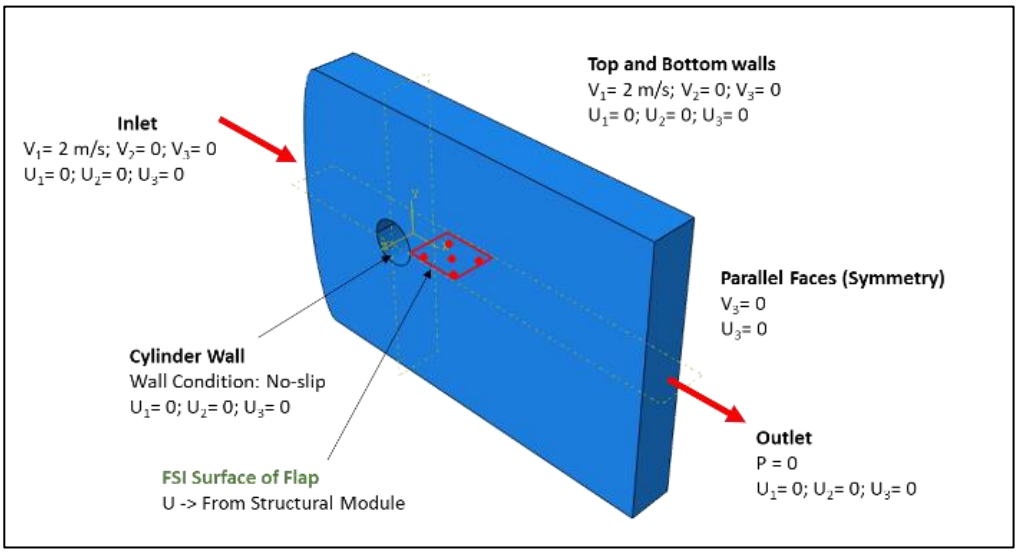


*Figure 3.1:* Boundary conditions imposed on the fluid domain

The deforming surface was defined through a "seam" crack. In this definition, overlapping nodes are placed at the specified crack region. Initially this remains closed, but during the analysis, it can open and deform as shown in Figure 3.2. This method is used in order to provide an FSI surface definition in the fluid domain, which

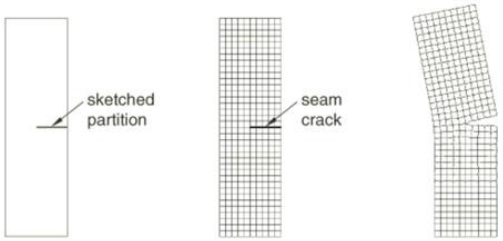


*Figure 3.2:* Seam crack definition
Source: ABAQUS 6.14 Documentation, (2014)

is equivalent to the two dimensional shell element formulation used in the structural domain.

### 3.1.4. Coupling Scheme

A partitioned FSI coupling scheme was implemented using an explicit, Gauss-Seidal algorithm. In this, the CSD module was the leading solver (i.e. it executes first) followed by the CFD module, which is the lagging solver. At each coupling cycle Abaqus/Standard was allowed to sub-cycle until a stable solution is reached and the displacement data was transferred to Abaqus/CFD through the Co-Simulation engine. The CFD module was allowed to proceed in "lock-steps", so that for each coupling cycle, Abaqus/CFD executed only one sub-cycle. The updated boundary conditions at the end of each coupling step was used in the solution assessment of the next coupling step, thus making this algorithm globally explicit. Time step size was determined based on the minimum of the step sizes required for CSD and CFD module. The whole procedure is given as a schematic in Figure 3.3.

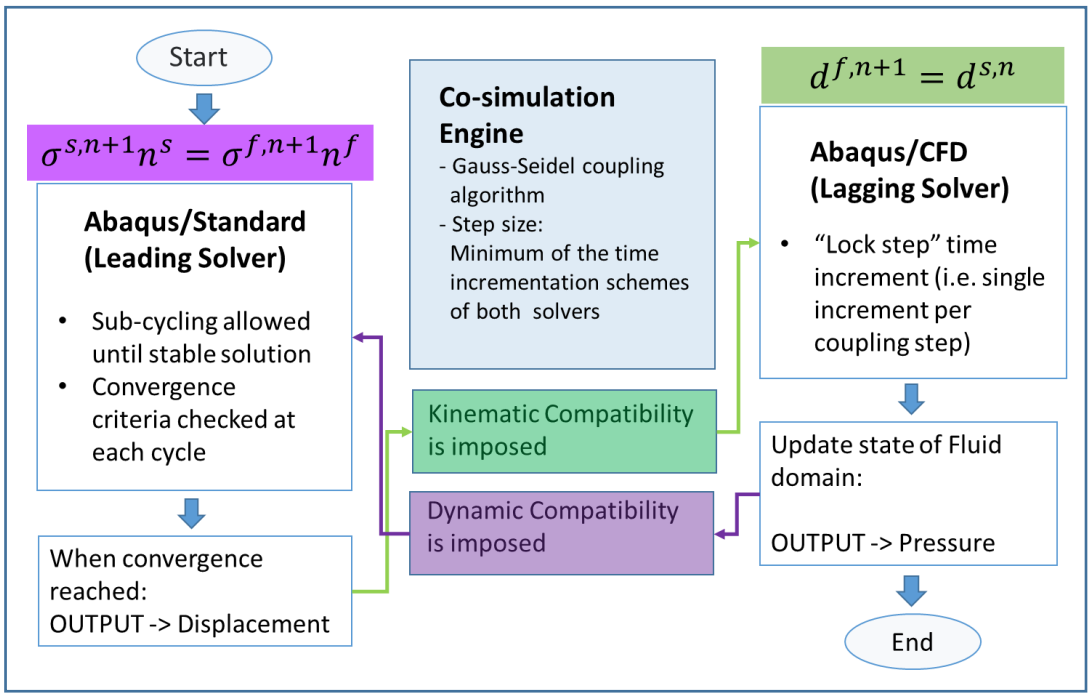


*Figure 3.3:* Coupling procedure for the co-execution of CSD and CFD modules

### 3.2. Model Specifications

In this section, the details of the developed model are presented. Commercial analysis package ABAQUS, version 6.14, and a workstation with Intel® Xeon® E5-2687W v3 processors and 128 GB of RAM were used for this work.

A partitioned/staggered FSI approach was chosen as this method requires lesser memory allocation and processing time compared to the monolithic approach discussed in Section 2.3.1. Also it can be easily implemented using commercially available codes. Structural Domain was analysed using Abaqus/Standard and the fluid domain was handled by Abaqus/CFD and data exchange was established at the interface through the Co-simulation Engine. Multiple processing cores were used in parallel, six for the CSD and fourteen for CFD. More cores were allocated for the fluid domain in order to handle the higher number of control volumes involved. Simulations were allowed to run for an average of 17 hours per trial.

#### 3.2.1. Verification Model

The standard benchmark study done by Turek & Hron (2006) on an elastic, flexible structure immersed in a laminar, incompressible flow was used for verification. The geometric details of the specified model is given in Figure 3.4. Polypropylene was used for the flexible structure and it was immersed in the viscous medium of glycerine.

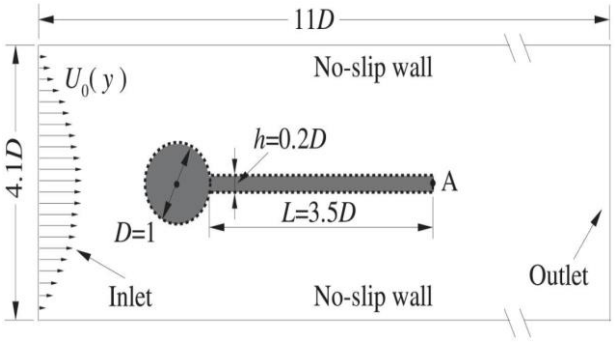


*Figure 3.4:* Schematic of benchmark study used by Turek and Hron (2006)

A diameter D of 10 mm was used. Combination of fluid and structural properties used for the study are given in Table 3.2. The model that was setup in the Abaqus

environment is shown in Figure 3.5 and more details are provided about each component in Section 3.2.2 and Section 3.2.3.

Table 3.2: Properties of structural and fluid components

| Material | Fluid | Structure |
|---|---|---|
| Fluid | Water (WAT) | Density = 1000 kg/m$^3$<br>Dynamic = 1x10$^{-3}$ Pa.s Viscosity |
| | Glycerine (GLY) | Density = 1000 kg/m$^3$<br>Dynamic = 1x10$^{-3}$ Pa.s Viscosity |
| Solid | Kapton (KAP) | Density = 1420 kg/m$^3$<br>Young's Modulus = 49 MPa<br>Poisson's ratio = 0.39 |
| | Polypropylene (PROP) | Density = 1000 kg/m$^3$<br>Young's Modulus = 140 MPa<br>Poisson's ratio = 0.4 |

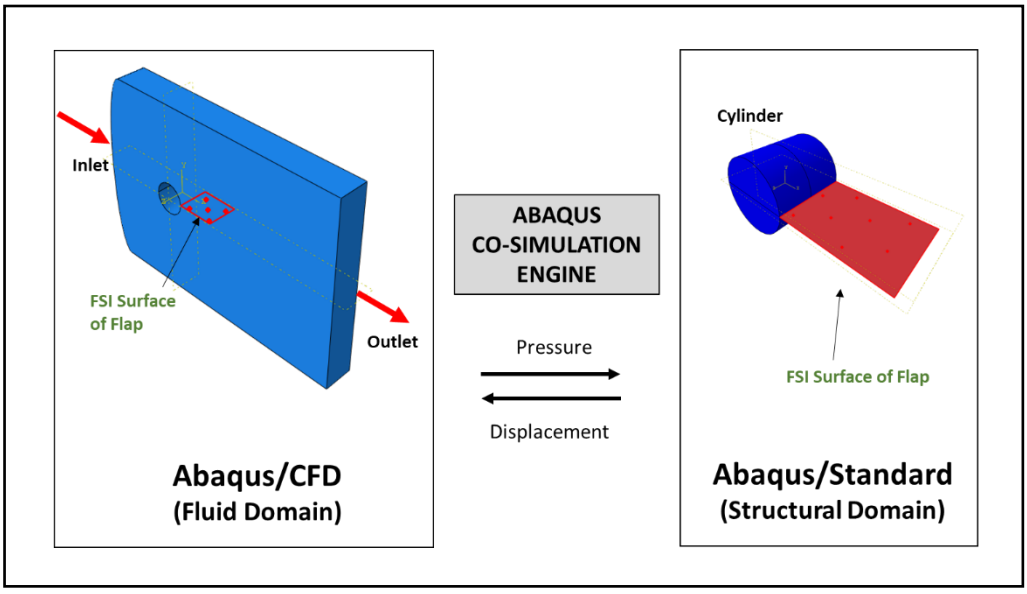


*Figure 3.5:* FSI setup implemented in ABAQUS environment

### 3.2.2. Structural Domain

Two element formulations were tested for the structural module. In Model 1 continuum shell elements were used and in all other methods 2D shell element formulation was used. The model details are summarized in Table 3.3.

A number of works before have used solid element formulation for FSI analysis as discussed in Section 2.3.2. (Nguyen et al., 2016) In this study, shell element formulation was chosen instead. If solid elements were used, second order elements or first order solid elements with at least four in the through thickness direction will be required to capture the bending behaviour. Both options are computationally expensive than a shell formulation for a very thin membranous structure. De Nayer et al. (2014) have used shell formulation in their work involving an in-house code, In the present work, the capabilities of the Abaqus software package was exploited. Abaqus/Standard offers thick, thin and general purpose elements for FEM analysis. Though geometrically the structure satisfies thin shell criteria, general purpose shell elements were used as recommended by the Abaqus 6.14 Documentation. Element S4 (four-noded, fully integrated, finite membrane strain element) and S4R (four-noded, finite membrane strain element with reduced integration), shown in Figure 3.6 were

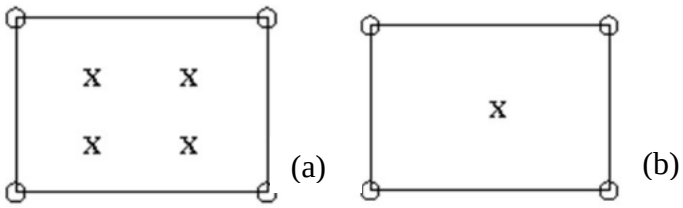


*Figure 3.6:* General-purpose element in Abaqus/Standad (a) S4 (b) S4R

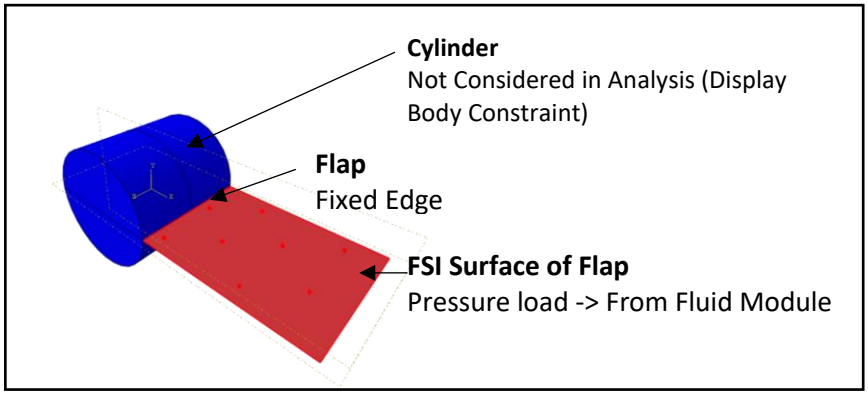


*Figure 3.7:* Structual model setup in Abaqus/Standard

considered. S4R was chosen with computational time as the main factor. Also, S4R is compatible with hyper-elastic material. Though this material model is not considered in the current study, having the flexibility to extend this model to that regime in future works was considered an added advantage.

The cylinder in the considered structural geometry was assumed to show rigid behaviour. Therefore it was modelled with a "Display body" constraint, which effectively removes it from the analysis and displays it as in Figure 3.7 only for visualization purposes. To address numerical difficulties encountered at different stages of the analysis, different combination of materials and formulations were attempted for the flexible structure and the fluid as given in Table 3.3.

Table 3.3: Different cases considered for FSI analysis

| **Model** | **Formulation** | **Fluid** |
|---|---|---|
| Model 1 | Continuum Shell | Fluid: GLY<br>Solid: PROP<br>U = 10 m/s |
| Model 2 | Shell | Fluid: GLY<br>Solid: PROP<br>U = 10 m/s |
| Model 3 | Shell | Fluid: GLY<br>Solid: PROP<br>U = 20 m/s |
| Model 3 | Shell | Fluid: GLY<br>Solid: KAP<br>U = 20 m/s |
| Model 4 | Shell | Fluid: WAT<br>Solid: KAP<br>U = 20 m/s |
| Model 5 (Creased membrane) | Shell | Fluid: WAT<br>Solid: KAP<br>U = 20 m/s |

### 3.2.3. Fluid Domain

Three dimensional, eight-noded continuum elements were used, the schematic representation of which is shown in Figure 3.8. The Spalart Allmaras turbulence model was used to capture the vortices generation close to the moving boundary. Initial turbulent kinematic eddy viscosity was set to $1x10^{-9}$ Pa.s. Backward Euler time integration with automatic time-stepping and a maximum CFL of 1 was used. Due to the flexible moving boundary involved in this analysis, a user defined pressure equation solver was used. The "Flexible generalized minimal residual solver" with Algebraic multi-grid preconditioning was used for this purpose. Residual smoothening was achieved through "Incomplete factorization method" and two pre-sweeps and two post-sweeps.

For Model 1 since continuum shells are used for the structural domain, it is introduced in the fluid domain as a three dimensional cut as shown in Figure 3.9. In Case 2 to Case 5 a two dimensional seam surface is introduced in the fluid domain to indicate the presence of the shell section as shown in Figure 3.9.

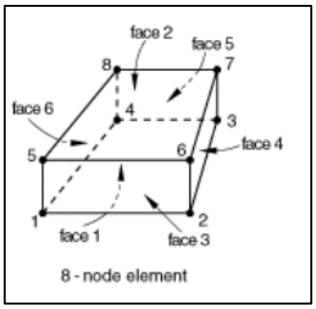


*Figure 3.8:* FC3D8 element in Abaqus/CFD

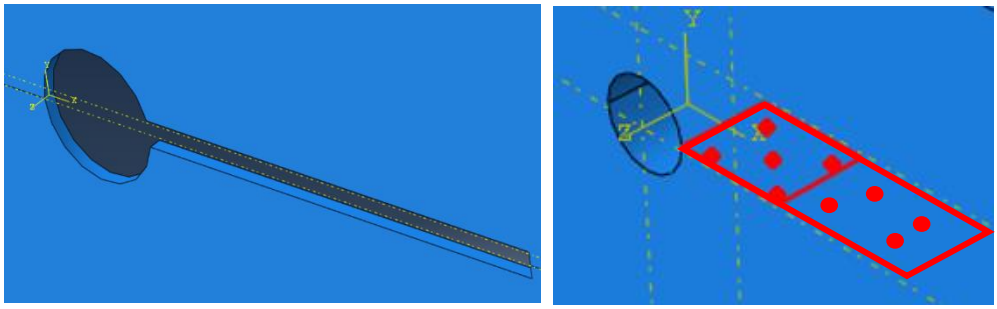

*Figure 3.9:* Three-dimensional cut in the fluid domain demarcating the fluid-structure interface

### 3.2.4. Verification of Fluid Domain

To verify the suitability of the fluid mesh, a standard simulation of "flow around a rigid cylinder" was initially performed and the results were compared qualitatively with the flow pattern expected at different Reynolds numbers as presented in Figure 3.9.

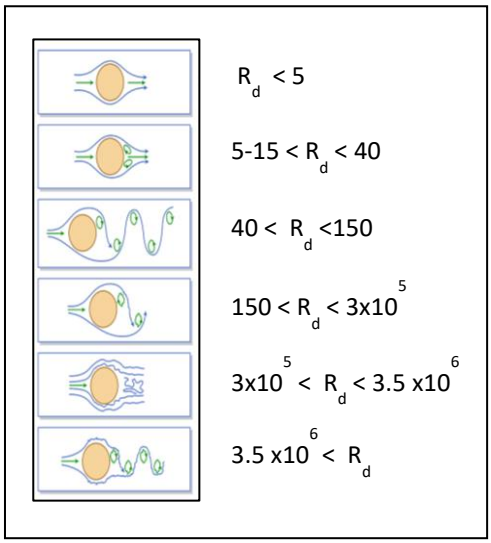


*Figure 3.10*: Flow patterns at different Reynolds numbers

**Trial 1**

First trial was performed with a mesh of 101700 control volumes. Element size was 2mm close to the moving boundary and 17mm further away. The different inflow velocities considered in order to cover different regimes of Reynolds number are given in Table 3.4.

Table 3.4: Cases considered for verification of fluid domain set-up

| | **Reynolds Number** | **Inflow Velocity (mm/s)** |
|---|---|---|
| CASE 1 | 0.038 | $4.77 \times 10^{-3}$ |
| CASE 2 | 50 | 6.27 |
| CASE 3 | 100 | 12.5 |
| CASE 4 | 195 | 24.5 |
| CASE 5 | 600 | 60 |

The flow patterns obtained from the simulation are given in Figure 3.11. These tally qualitatively with the expected flow patterns, confirming that the setup is consistent numerically. Further investigations were done comparing the vortex shedding period. The Strouhal Number was calculated using Equation 3.18 based on the Reynolds number, a relationship contrived by Rayleigh in 1896. Then using this value, Equation 3.19 was exploited to calculate the period of oscillation. This was compared with the period obtained from the numerical simulation. The comparison is presented in Table 3.4.

$$St = 0.195 \times \left(1 - \frac{20.1}{Re}\right) \tag{3.18}$$

$$f = \frac{St \, x \, U}{d} \tag{3.19}$$

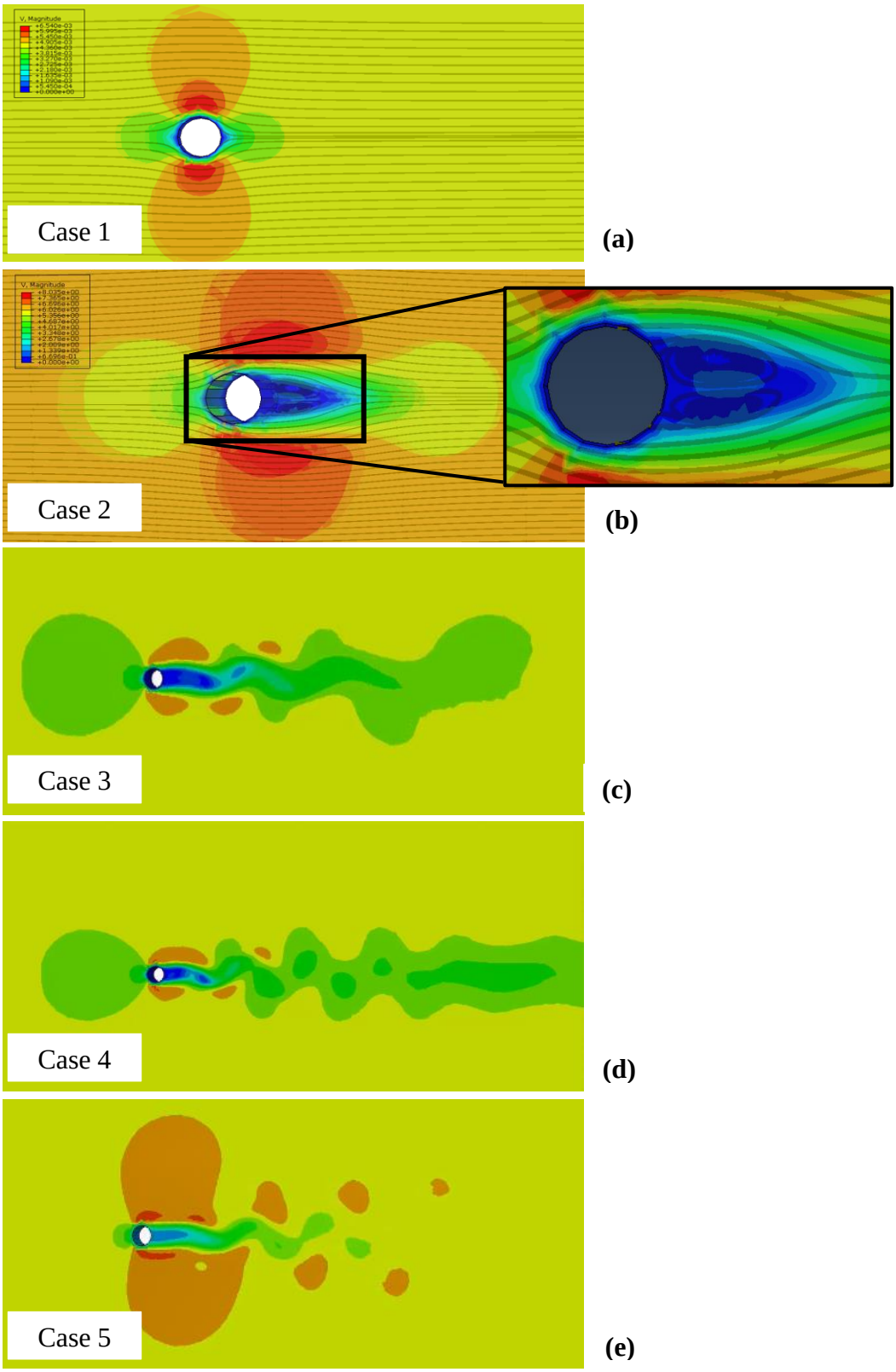


*Figure 3.11:* Results from verification of fluid domain based on the simulation of "flow around a rigid cylinder" (a) Re << 5 (b) Re ≈ 60 (c) Re ≈ 100 (d) Re >> 100 (e) Re = 600

Table 3.5: Comparison of period of oscillation from calculation and simulation

| Case | Re | $S_t$ | $F_{calculated}$ | $T_{calculated}$ | $T_{simulation}$ | Error % |
|---|---|---|---|---|---|---|
| 3 | 100 | 0.156 | 0.195 | 5.1 | 4.8 | 5.8% |
| 4 | 195 | 0.175 | 0.428 | 2.3 | 2.1 | 8.7% |
| 5 | 600 | 0.189 | 15.1 | 0.066 | 0.08 | 21% |

Comparing the difference in the period of oscillation calculated and obtained from simulation, it can be seen that the percentage of error increases with increasing Reynolds number. Since the Reynolds numbers considered for the current work were in the range of Case 3 and Case 4, this mesh was considered suitable.

However, when implemented in the FSI framework, this gave a response characterised by highly random vibratory oscillations, as shown in Figure 3.12. Further investigation revealed that the structural response was being transferred mainly through the lower face of the FSI surface, thus giving the higher amplitude of oscillation only in that direction, as shown in Figure 3.12. The reason for this was identified as the ill-defined mesh and a finer one was used in obtaining the results in Chapter 4. More details on the mesh are presented in Appendix A.

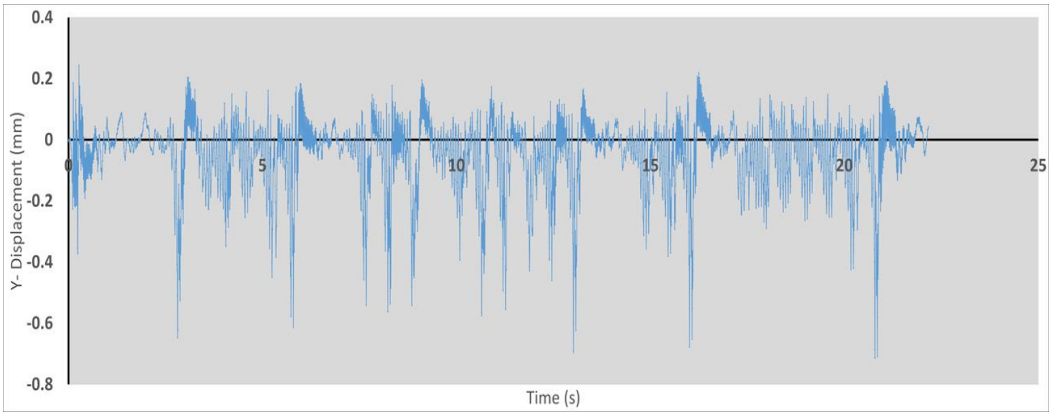


*Figure 3.12:*Displacement of the free end of the flap in the y-direction

# CHAPTER IV

## 4. RESULTS AND DISCUSSION

The results from the implementation of the different cases indicated in Section 3.2 are presented here, analysing the feasibility of using the different methods covered in each case. Section 4.1 focuses on the simulation of an uncreased, thin, flexible structure immersed in a low Reynolds number flow. Both continuum shell and conventional shell formulations were adopted and the latter was chosen owing to the lesser processing time required. The behaviour of two structural materials, polypropylene and kapton, were also studied. In the next section, the effect of the presence of a crease on the flow path of the fluid was studied and was compared with that of a similar case in the previous section.

### 4.1. Uncreased Membrane

A description of each model is given in Table 3.4. **Model 1** was not feasible due to the computational time required for processing. In contrast to the conventional shell that uses a reference surface to perform the numerical calculations, continuum shell considers the three dimensional nodal geometry. Owing to the inactive rotational degree of freedom in this formulation, it is effectively modelled like a continuum solid element. But the overall behaviour being similar to conventional shell, it provides a faster solution procedure than solids. However, in the case of an FSI problem, this was not computationally feasible with the available resources. Thus, the conventional shell formulation (hereinafter referred to as shell) will be considered in the succeeding sections.

**Model 2** was analysed using the shell formulation. The resulting displacements in the x and y directions were compared with that presented by Turek and Hron (2006). This corresponds with the FSI 2 model presented by the authors. It must be noted that the developed model is $1/10^{th}$ of the dimensions used by Turek and Hron. The oscillation amplitudes in x and y directions are compared based on a direct geometric scaling down of the values from literature. When scaling down geometric, kinematic

and dynamic similarities should be enforced. If geometric and dynamic similarities are preserved, kinematic similarity is automatically satisfied, since it describes the motion of the structure resulting from the forces acting on it (*General Modelling and Scaling Laws*, n.d.). In this case, all dimensions of the setup were uniformly scaled down to $1/10^{th}$ as mentioned earlier. Reynolds number was preserved ensuring that the ratio of inertial to viscous force was same. Pressure forces are a direct function of the area (i.e. the length). Thus this is satisfied by the developed model. Elastic fluid forces of the fluids considered in this study are negligible, which eliminates the need to compare the Mach number. Effect of gravitational forces was considered negligible. Thus dynamic similarity conditions are satisfied. This enables the comparison of amplitudes through direct scaling down as described before. The results are given in Table 4.1. It can be seen that the amplitudes are much less than expected. However, it must be noted that the simulation has proceeded only 0.046s, compared to the 20s defined for this flow step in the input, to get comprehensive response data. Also, Figure 4.2 shows that the displacement is still in developing stage, showing an increasing trend. The simulation should be allowed to proceed for sufficient amount of time until a stabilized oscillation is obtained.

**Model 3** corresponds to the FSI 3 model in the benchmark test referred to earlier. The inlet velocity is increased from 10 m/s to 20 m/s, resulting in a Reynolds number of 200. The flow becomes more turbulent with a diverging vortex street as shown in Figure 4.1. The higher amplitude of oscillation in the simulation is due to the undamped trailing edge. To get a stable response a trailing mass has been used in the benchmark study, which is not accounted for in the simulation.

Next, to investigate the capability of the developed simulation technique to handle a structural material of lower stiffness, **Model 4** was analysed with kapton as the flexible component. This material was chosen as it is commonly used in MAV wing designs. This initially gives a highly random oscillatory movement (Figure 4.2) as expected due to the low stiffness of the structure. It is anticipated that if the simulation is allowed to proceed for a sufficient time, it will reach steady state.

Table 4.1: Comparison of FSI simulation with benchmark test

| **Model** | **Turek and Hron (2006) (Scaled down by 1/10$^{th}$)** | | **Simulation** | |
|---|---|---|---|---|
| | $A_x$ | $A_y$ | $A_x$ | $A_y$ |
| Model 2 | −1.45±1.24 | 1.23 ± 80.6 | 0.02 | 0.00 ± 0.45 |
| Model 3 | −0.27 ± 0.25 | 0.15 ± 3.44 | 0.92 ± 0.82 | 0.00 ± 6.5 |

Note: 'A' is the amplitude of the sinusoidal displacement curve. It is expressed as a displacement in the positive and negative direction, starting from a mean value, given by the first term in the expressions for amplitudes.

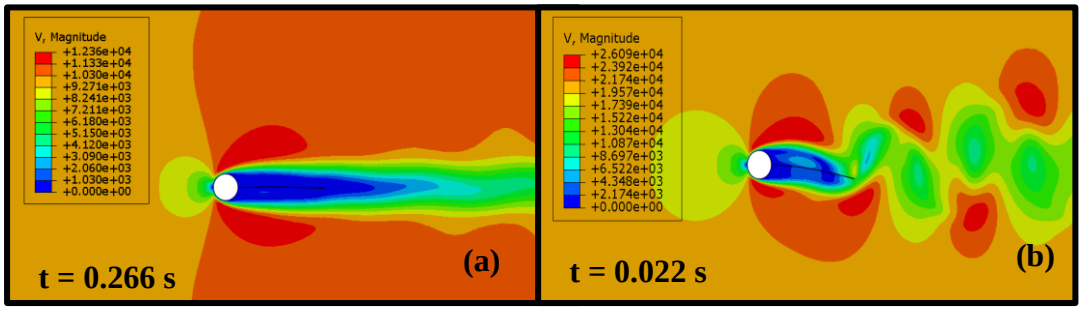


*Figure 4.1:* Velocity plot for inlet velocity (a) 10 m/s (b) 20 m/s

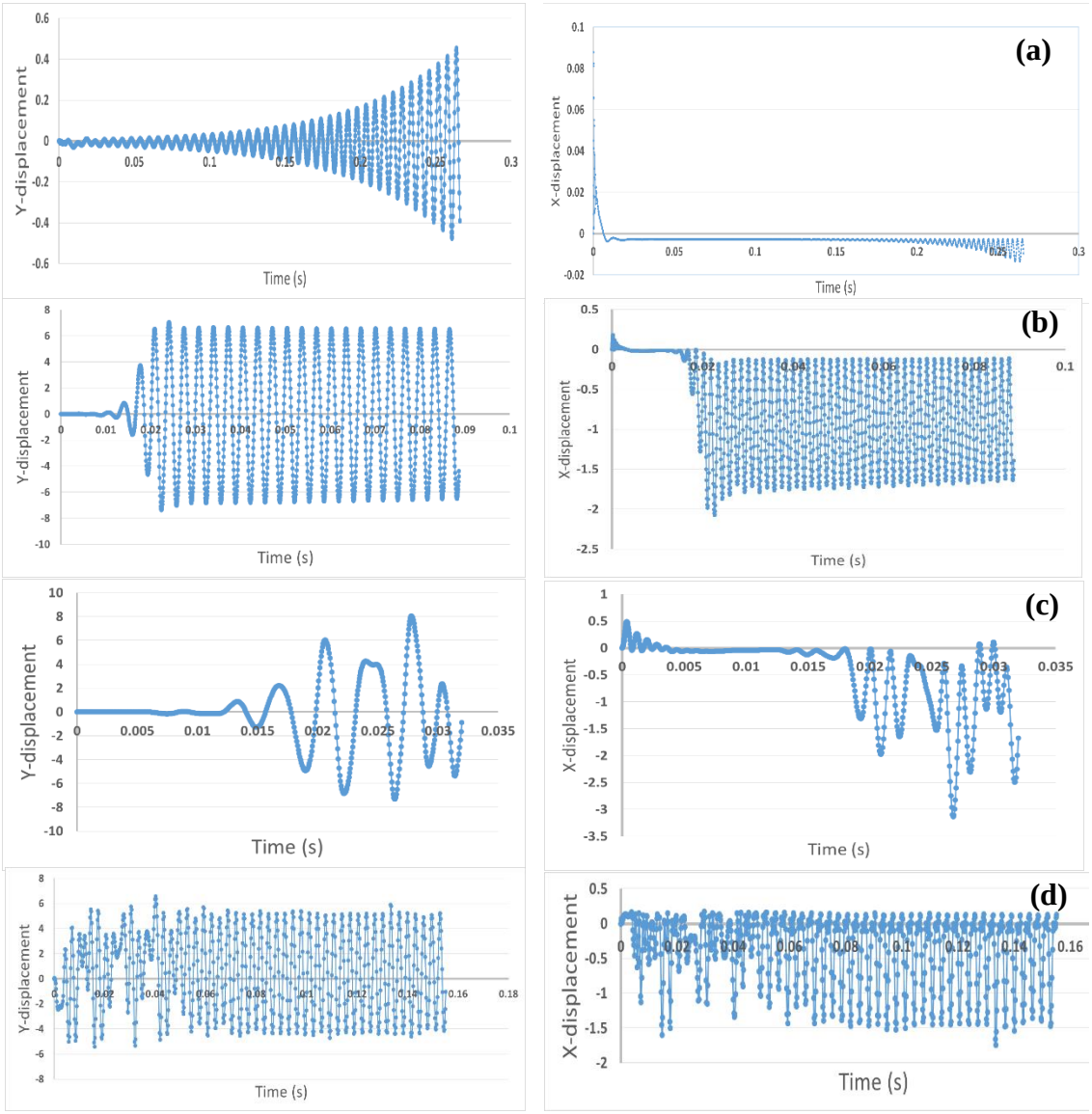


*Figure 4.2:* Displacement of point A (Fig. 3.4) in X and Y direction for: (a) Model 2 (b) Model 3 (c) Model 4 (d) Model 5. Note: All displacement values are in millimetres.

### 4.2. Creased Membrane

**Model 5** was implemented in a manner similar to the previous models, but with a crease line introduced parallel to the axis of the cylinder. A simplified crease geometry as the one shown in Figure 4.3 was used. A detailed study in the lines of crease modelling can be found in the works of Dharmadasa & Mallikarachchi (2016) and Mierunalan & Mallikarachchi (2017). Further, details of using an "effective elastic modulus" in the crease region to account for the change in structural response is discussed by Cai et al. (2017). Such intricacies were not included in the present study. Rather, Model 5 was used as an initial study to observe the change in flow pattern due to the presence of a creased thin membrane from a purely geometric perspective.

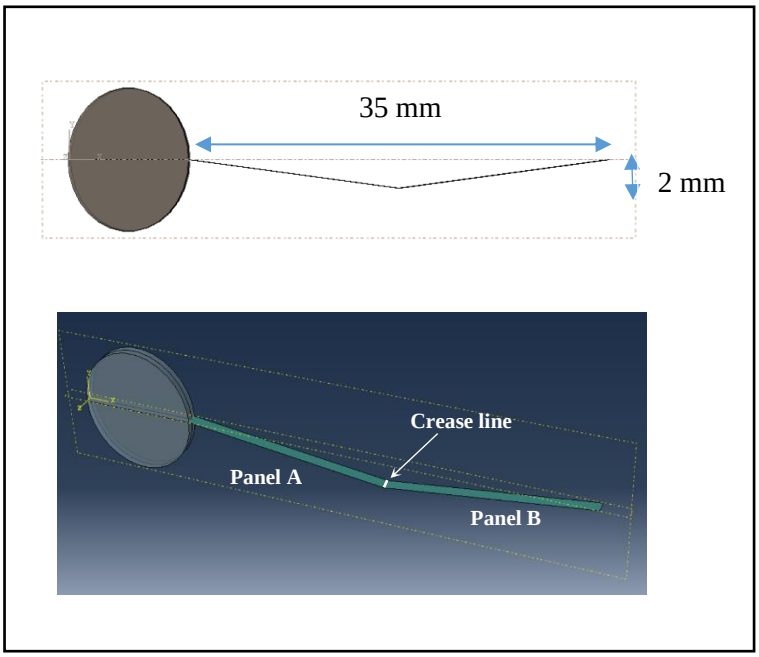


*Figure 4.3:* Crease geometry used in the study

The deformed profiles in Figure 4.5 clearly shows a difference in the response of a creased and uncreased geometry. While the uncreased membrane exhibited a mixed mode 1 and mode 2 type vibratory deformation, the creased one displayed a comparatively stiffer response. In the latter case, the movement can be described by considering panel B as a cantilevered section attached to moving points on the crease-line, while the translation of the crease itself is governed by panel A.

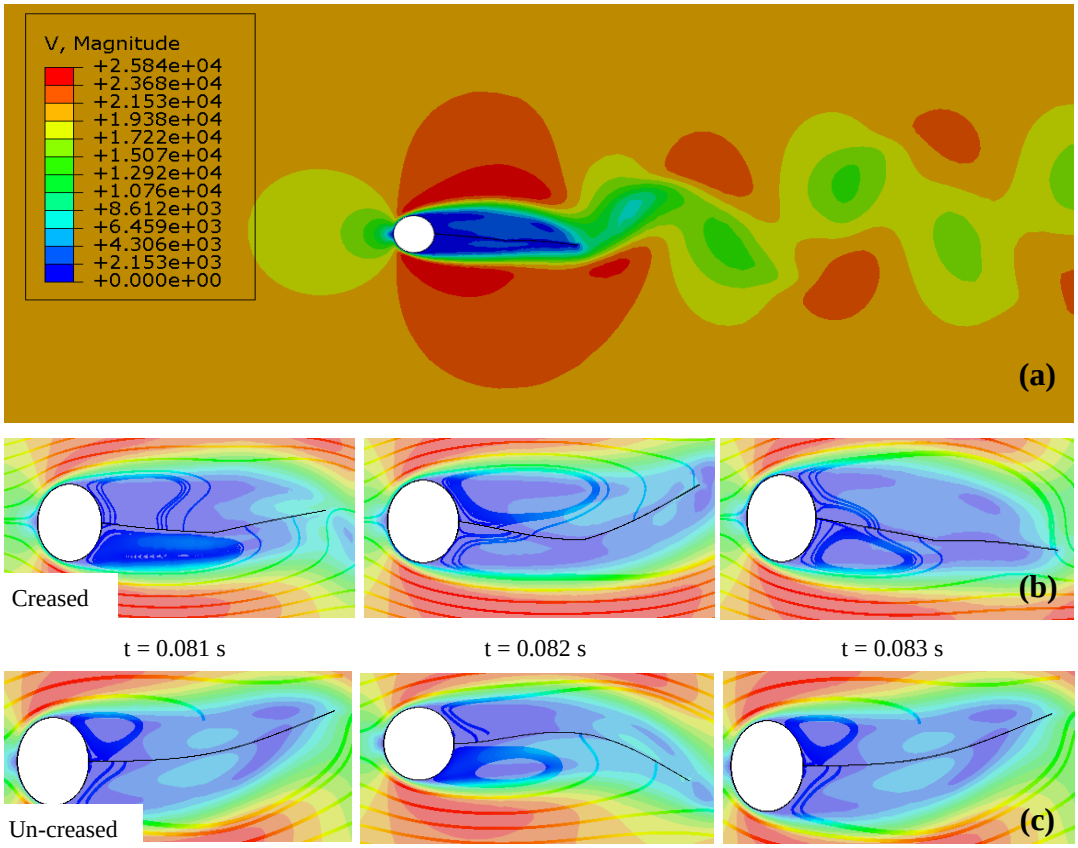


*Figure 4.4:* Comparison of flow over creased and uncreased membrane (a) velocity profile of creased membrane; Time history of streamlines in (a) creased (b) uncreased structure

The difference in vortex generation between the two geometries is shown in the vorticity plots given in Figure 4.5. Vorticity indicates the number of rotations per second. It is one of the important phenomena that starts off an oscillatory motion in FSI problems.

It is also the key mechanism that governs insect flight as discussed in Section 2.1. Insect wings employ various mechanisms to keep the instant0aneous leading edge vortex (LEV) attached to the wing for a longer period. Creases, in theory, seem geometrically suitable to capture and retain them for a longer period.

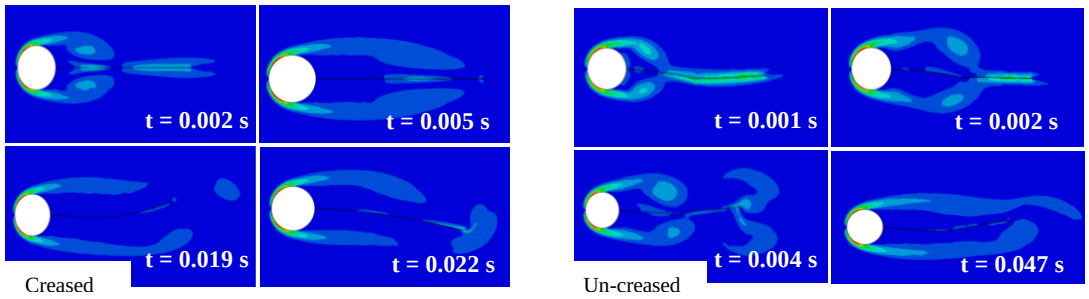


*Figure 4.5*: Vorticity plot for (a) an uncreased membrane (b) a creased membrane

However, when the vorticity was plotted over the length of the wing for three successive time frames as shown in Figure 4.5, the uncreased one displayed a more vortical flow. This is due the stiffer behaviour of the creased model, imparting lesser obstruction to the flow. However, it should be noted that neither the exact rotational stiffness at the crease-line nor the stiffness of the region adjoining it have been incorporated in this model. Also, the above observation is not sufficient to derive conclusions on the vortex retention time as that requires the study of the vortices over a longer time frame. It may be possible that, though the strength of the resulting vortex itself is comparatively lesser in creased membranes, it might still be sufficient to keep an insect scale object afloat and by retaining the vortex longer, such membranes may perform better in sustaining the flight.

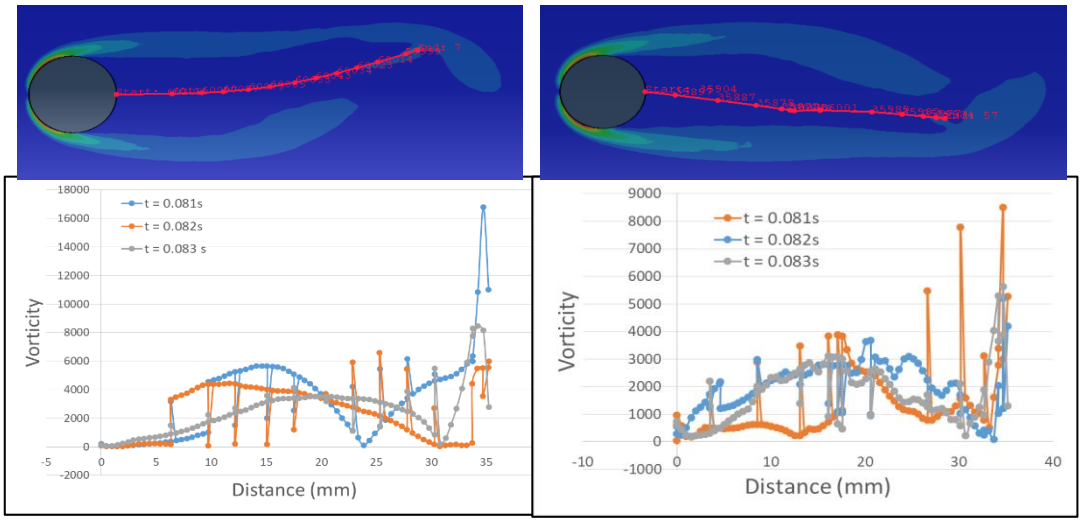


*Figure 4.6:* Vorticity plot along the length of the (a) Uncreased plate (b) Creased plate

# CHAPTER V

## 5. CONCLUSION AND FUTURE WORK

### 5.1. Conclusion

A detailed study on performing a fluid-structure interaction analysis involving a thin, flexible membrane immersed in a flowing fluid was conducted and a technique was proposed based on the commercially available ABAQUS multi-physics environment. Initially, the suitability of the method was investigated. Based on a rigorous review of the theoretical background, the ABAQUS code was verified to be appropriate for the purpose.

The FSI framework was implemented in three stages. First, the structural domain was developed. Shell and continuum shell formulations were used in order to decide on the optimum formulation.

Next, the fluid domain was developed using a Spalart-Allmaras turbulence model and was verified qualitatively based on the variation in flow around a rigid cylinder with Reynolds Number. Finally, both aforementioned domains were coupled using an explicit Gauss-Seidal scheme through the ABAQUS Co-simulation Engine. This was verified against a standard benchmark study conducted by Turek and Hron (2006), which involves a cylinder immersed in a laminar flow with a thin, flexible flap attached to its downstream side. A precise reproduction of the results of the benchmark case was not achieved in the above simulation. However, salient features like the vortex street and the streamline were captured. Further, the suitability of using a two dimensional shell formulation together with a 2D seam surface crack in the fluid domain was proved.

As the next step, a membrane with a predefined crease geometry was tested in the same FSI framework. Due to the stiffer behaviour of the creased model, the vortical behaviour of membrane was limited. Also the significance of incorporating rotational stiffness at the crease-line and the stiffness of the region adjoining it was identified. Further, in order to assess the aerodynamic performance, a study over a

longer time period is required. Thus more work has to be performed to bring down the processing time.

## 5.2. Future Work

This section presents a brief overview of possible avenues to extend this work in order to assess the aerodynamic performance of a deployable wing. The following areas require special attention.

- Mesh sensitivity study for both fluid and structural domain as well as the FSI framework
- Include hyper-elastic material model
- Introduce a crease model

A brief theoretical background and the initial analysis performed in the area of crease modelling is described in Section 6.1.1.

### 5.2.1. Crease Modelling through Plastic Damage

A crease can be modelled as a plastic damage of the material, which has left an irreversible kink in the geometry relative to its initial shape, i.e. if sufficient stress is applied such that the yield stress is surpassed, plastic yielding occurs along the crease line preventing it from returning to its original shape.

This concept can be implemented through FEM by following the procedure illustrated by Figure 6.2 and Figure 6.3.

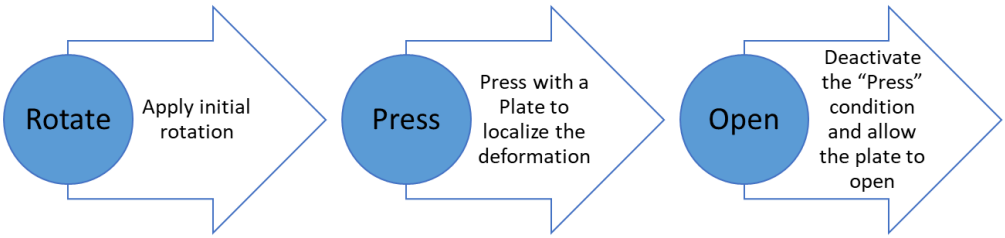


*Figure 5.1:* Procedure to introduce crease as a plastic deformation in an initially flat plate

This method requires a mesh of high refinement near the crease line and comprehensive material data describing the progressive damage. A detailed study was not performed in this area as it is beyond the scope of the project. However, in order to assess the aerodynamic performance of a deployable insect-scale wing, the above method should be studied further.

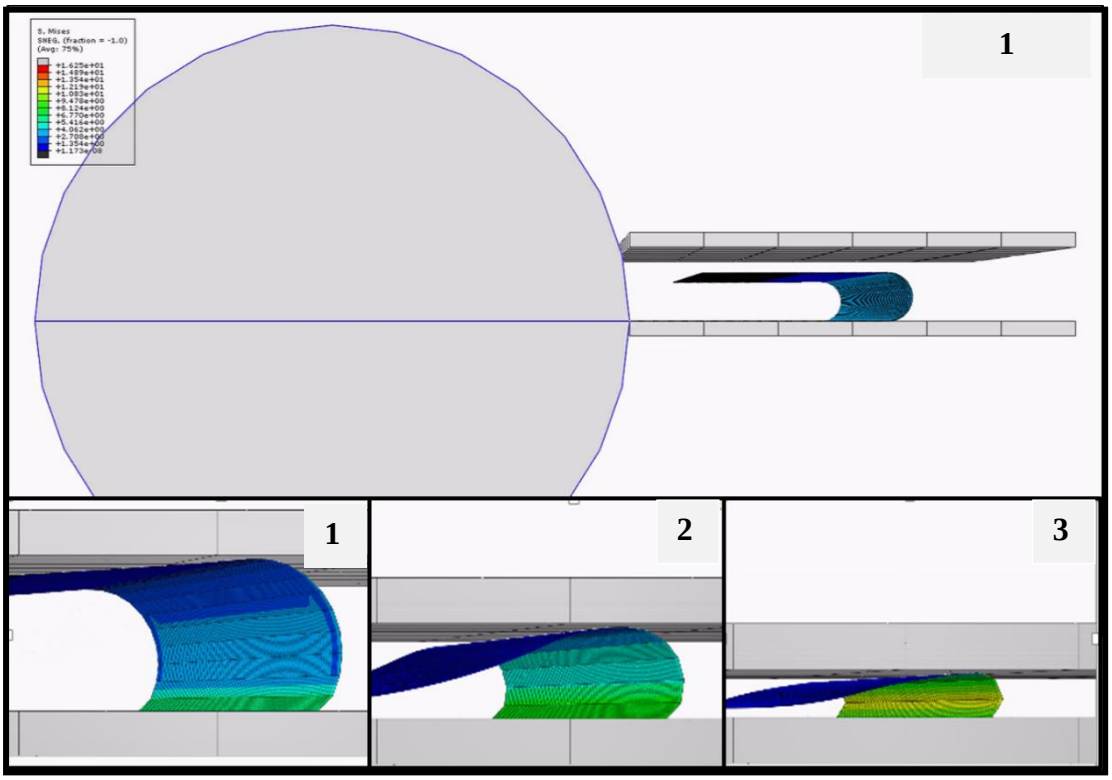


*Figure 5.2:* Localizing a plastic deformation by pressing between two rigid plates

# REFERENCES


Abaqus. (2014). Analysis User's Guide (ver 6.14). In *Abaqus Documentation*. Providence, Rhode Island: Dassault Systemes Simulia Corp.

Alexander, D. E. (2004). *Nature's Flyers: Birds, Insects, and the Biomechanics of Flight*. Johns Hopkins University Press.

Brackenbury, J. H. (1994). Wing folding and free-flight kinematics in Coleoptera (Insecta): a comparative study. *Journal of Zoology*, *232*(2), 253–283. https://doi.org/10.1111/j.1469-7998.1994.tb01572.x

Cai, J., Ren, Z., Ding, Y., Deng, X., Xu, Y., & Feng, J. (2017). Deployment simulation of foldable origami membrane structures. *Aerospace Science and Technology*, *67*(April), 343–353. https://doi.org/10.1016/j.ast.2017.04.002

Chen, Y., Feng, H., Ma, J., Peng, R., & You, Z. (2016). Symmetric waterbomb origami. *Proceedings of the Royal Society A: Mathematical, Physical and Engineering Science*, *472*(2190), 20150846. https://doi.org/10.1098/rspa.2015.0846

Combes, S. A. (2010). Materials, Structure, and Dynamics of Insect Wings as Bioinspiration for MAVs. *Encyclopedia of Aerospace Engineering*, 1–10. https://doi.org/10.1002/9780470686652.eae404

De Nayer, G., Kalmbach, A., Breuer, M., Sicklinger, S., & Wüchner, R. (2014). Flow past a cylinder with a flexible splitter plate: A complementary experimental-numerical investigation and a new FSI test case (FSI-PfS-1a). *Computers and Fluids*, *99*, 18–43. https://doi.org/10.1016/j.compfluid.2014.04.020

Deiters, J., Kowalczyk, W., & Seidl, T. (2016). Simultaneous optimisation of earwig hindwings for flight and folding. *Biology Open*, *5*(5), 638–644. https://doi.org/10.1242/bio.016527

Dharmadasa, B. Y., & Mallikarachchi, H. M. Y. C. (2016). " Finite Element Simulation of Thin Folded Membranes ", (December).

Donea, J., Huerta, A., Ponthot, J.-P., & Rodríguez-Ferran, A. (2004). Arbitrary Lagrangian-Eulerian Methods. In E. Stein, R. Borst, & T. J. . Hughes (Eds.), *Encyclopedia of Computational Mechanics: Volume 1*. John Wiley & Sons, Ltd. Retrieved from https://www.wiley.com/legacy/wileychi/ecm/pdfs/Volume_1_Chapter_14.pdf

Ellington, C. P., Van Berg, C. Den, Willmott, A. P., & Thomas, A. L. R. (1996). Leading-edge vortices in insect flight. *Nature*, *384*(6610), 626–630. https://doi.org/10.1038/384626a0

Elsayed, E. A., & Basily, B. (2004). A continuous folding process for sheet materials. *International Journal of Materials and Product Technology*, *21*(1/2/3), 217. https://doi.org/10.1504/IJMPT.2004.004753

Fernández, M. A. (2011). Coupling schemes for incompressible fluid-structure interaction: implicit, semi-implicit and explicit. *SeMA Journall: Boletin de La Sociedad Española de Matemática Aplicada, Springer*, *55*(1), 59–108. https://doi.org/10.1007/BF03322593

Forbes, W. T. M. (1924). How a Beetle Folds its Wings. *Psyche (New York)*, *31*(6), 254–258. https://doi.org/10.1155/1924/68247

*General Modelling and Scaling Laws*. (n.d.). Retrieved from http://www.ivt.ntnu.no/imt/courses/tmr7/lecture/Scaling_Laws.pdf

Ha, N. S., Truong, Q. T., Goo, N. S., & Park, H. C. (2013). Biomechanical properties of insect wings: The stress stiffening effects on the asymmetric bending of the Allomyrina dichotomabeetle's hind wing. *PLoS ONE*, *8*(12), 1–10. https://doi.org/10.1371/journal.pone.0080689

Haas, F., & Wootton, R. J. (1996). Two Basic Mechanisms in Insect Wing Folding. *Proceedings of the Royal Society B: Biological Sciences*, *263*(1377), 1651–1658. https://doi.org/10.1098/rspb.1996.0241

Jenkins, C. H. (1996). Nonlinear Dynamic Response of Membranes: State of the Art - Update. *Applied Mechanics Reviews*, *49*(10S), S41–S48. Retrieved from http://dx.doi.org/10.1115/1.3101975

Jongerius, S. R., & Lentink, D. (2010). Structural Analysis of a Dragonfly Wing. *Experimental Mechanics*, *50*(9), 1323–1334. https://doi.org/10.1007/s11340-010-9411-x

Lebée, A. (2015). From Folds to Structures, a Review. *International Journal of Space Structures*, *30*(2), 55–74. https://doi.org/10.1260/0266-3511.30.2.55

Lian, Y., Shyy, W., Ifju, P., & Verron, E. (2002). A Computational Model for Coupled Membrane-Fluid Dynamics. In *32nd AIAA Fluid Dynamics Conference and Exhibit*. American Institute of Aeronautics and Astronautics. https://doi.org/doi:10.2514/6.2002-2972

Liu, H. (2009). Integrated modeling of insect flight: From morphology, kinematics to aerodynamics. *Journal of Computational Physics*, *228*(2), 439–459. https://doi.org/10.1016/j.jcp.2008.09.020

Liu, H., & Kawachi, K. (1998). A Numerical Study of Insect Flight. *J.~Comput.\ Phys.*, *146*, 124–156.

Liu, M., Huang, J., & Wang, Y. (2017). Analysis of wrinkled membrane structures based on a wrinkle-wave model. *AIP Advances*, *7*(1). https://doi.org/10.1063/1.4974248

Madangopal, R., Khan, Z. A., & Agrawal, S. K. (2005). Biologically Inspired Design Of Small Flapping Wing Air Vehicles Using Four-Bar Mechanisms And Quasi-steady Aerodynamics. *Journal of Mechanical Design*, *127*(4), 809. https://doi.org/10.1115/1.1899690

Mahadevan, L. (2005). Self-Organized Origami. *Science*, *307*(5716), 1740–1740. https://doi.org/10.1126/science.1105169

Mierunalan, S., & Mallikarachchi, H. M. Y. C. (2017). Prediction of creased geometry of thin folded membranes using finite element analysis. *3rd International Moratuwa Engineering Research Conference, MERCon 2017*, 283–287. https://doi.org/10.1109/MERCon.2017.7980496

Mooney, M. (1940). A theory of large elastic deformation. *Journal of Applied Physics*,

*11*(9), 582–592. https://doi.org/10.1063/1.1712836

Mountcastle, A. M., & Combes, S. A. (2013). Wing flexibility enhances load-lifting capacity in bumblebees. *Proceedings of the Royal Society B: Biological Sciences*, *280*(1759), 20130531–20130531. https://doi.org/10.1098/rspb.2013.0531

Newman, B. G. (1987). Aerodynamic theory for membranes and sails. *Progress in Aerospace Sciences*, *24*(1), 1–27. https://doi.org/10.1016/0376-0421(87)90005-4

Nguyen, T. T., Shyam Sundar, D., Yeo, K. S., & Lim, T. T. (2016). Modeling and analysis of insect-like flexible wings at low Reynolds number. *Journal of Fluids and Structures*, *62*, 294–317. https://doi.org/10.1016/j.jfluidstructs.2016.01.012

Peskin, C. S. (1972). Flow patterns around heart valves: A numerical method. *Journal of Computational Physics*, *10*(2), 252–271. https://doi.org/10.1016/0021-9991(72)90065-4

Rowlatt, C. F., & Phillips, T. N. (2016). A spectral element formulation of the immersed boundary method for Newtonian fluids. *Computer Methods in Applied Mechanics and Engineering*, *298*, 29–57. https://doi.org/10.1016/J.CMA.2015.08.010

Saito, K., Nomura, S., Yamamoto, S., Niyama, R., & Okabe, Y. (2017). Investigation of hindwing folding in ladybird beetles by artificial elytron transplantation and microcomputed tomography. *Proceedings of the National Academy of Sciences*, *114*(22), 5624–5628. https://doi.org/10.1073/pnas.1620612114

Saito, K., Tsukahara, A., & Okabe, Y. (2015). New Deployable Structures Based on an Elastic Origami Model. *Journal of Mechanical Design*, *137*(2), 021402. https://doi.org/10.1115/1.4029228

Selvadurai, A. P. S., & Shi, M. (2012). Fluid pressure loading of a hyperelastic membrane. *International Journal of Non-Linear Mechanics*, *47*(2), 228–239. https://doi.org/10.1016/j.ijnonlinmec.2011.05.011

Shyy, W., Lian, Y., Tang, J., Viieru, D., & Liu, H. (2007). *Aerodynamics of low reynolds number flyers*. *Aerodynamics Of Low Reynolds Number Flyers* (Vol.

9780521882). Cambridge: Cambridge University Press. https://doi.org/10.1017/CBO9780511551154

Smith, M. J. C., Wilkin, P. J., Williams, M. H., & Lafayette, W. (1996). The advantages of an unsteady panel method in modelling the aerodynamic forces on rigid flapping wings. *Journal of Experimental Biology*, *1083*, 1073–1083. https://doi.org/JEB9635

Taya, M., Van Volkenburgh, E., Mizunami, M., & Nomura, S. (2016). Design of autonomous systems. In *Bioinspired Actuators and Sensors* (pp. 436–458). Cambridge: Cambridge University Press. https://doi.org/10.1017/CBO9781107588271.008

Tessler, A., Sleight, D. W., & Wang, J. T. (2003). Nonlinear shell modeling of thin membranes with emphasis on structural wrinkling. *44th AIAA/ASME/ASCE/AHS Structures, Structural Dynamics, and Materials Conference*, (April), 1–11. https://doi.org/10.2514/6.2003-1931

Thill, C., Downsborough, J. D., Lai, S. J., Bond, I. P., & Jones, D. P. (2010). Aerodynamic study of corrugated skins for morphing wing applications. *Aeronautical Journal*, *114*(1154), 237–244. https://doi.org/10.1017/S0001924000003687

Tian, F.-B., Dai, H., Luo, H., Doyle, J. F., & Rousseau, B. (2014). Fluid–structure interaction involving large deformations: 3D simulations and applications to biological systems. *Journal of Computational Physics*, *258*, 451–469. https://doi.org/10.1016/j.jcp.2013.10.047

Turek, S., & Hron, J. (2006). Proposal for numerical benchmarking of fluid-structure interaction between an elastic object and laminar incompressible flow. In H. Bungartz & M. Schäfer (Eds.), *Lecture Notes in Computational Science and Engineering:Fluid-Structure Interaction* (pp. 371–385). Berlin, Heidelberg: Springer Berlin Heidelberg. https://doi.org/10.1007/3-540-34596-5_15

Viieru, D., Tang, J., Lian, Y., Liu, H., & Shyy, W. (2006). Flapping and Flexible Wing Aerodynamics of Low Reynolds Number Flight Vehicles. *44th AIAA Aerospace*

*Sciences Meeting and Exhibit*, (January), 1–18. https://doi.org/10.2514/6.2006-503

Wood, R., Nagpal, R., & Wei, G. Y. (2013). Flight of the robobees. *Scientific American*, *308*(3), 60–65. https://doi.org/10.1038/scientificamerican0313-60

Wootton, R. (1999). How flies fly. *Nature*, *400*(July), 112–113. https://doi.org/10.1038/21998

Wootton, R. J. (1979). Function, homology and terminology in insect wings. *Systematic Entomology*, *4*(1), 81–93. https://doi.org/10.1111/j.1365-3113.1979.tb00614.x

Wootton, R. J. (1981). Support and deformability in insect wings. *Journal of Zoology*, *193*(4), 447–468. https://doi.org/10.1111/j.1469-7998.1981.tb01497.x

Zhao, L., Huang, Q., Deng, X., & Sane, S. P. (2010). Aerodynamic effects of flexibility in flapping wings. *Journal of the Royal Society, Interface*, *7*(44), 485–97. https://doi.org/10.1098/rsif.2009.0200

# APPENDIX

## A. MESH DETAILS

TRIAL 1

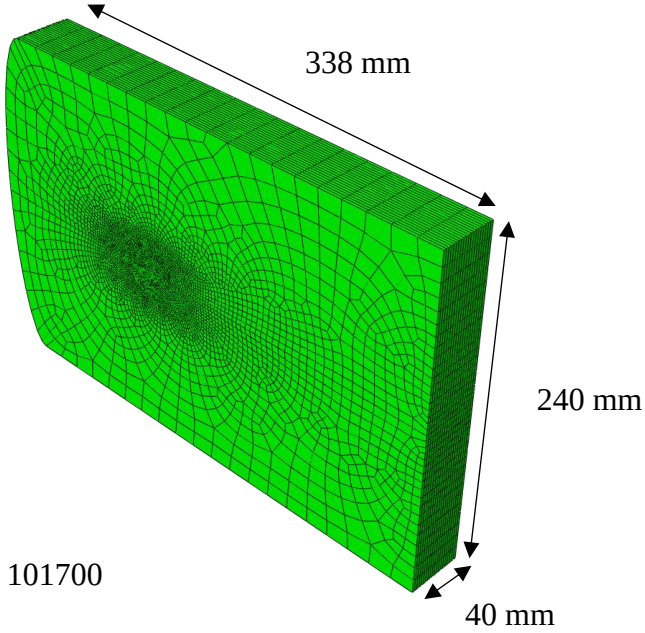


**Fluid Domain**

Number of elements: 101700

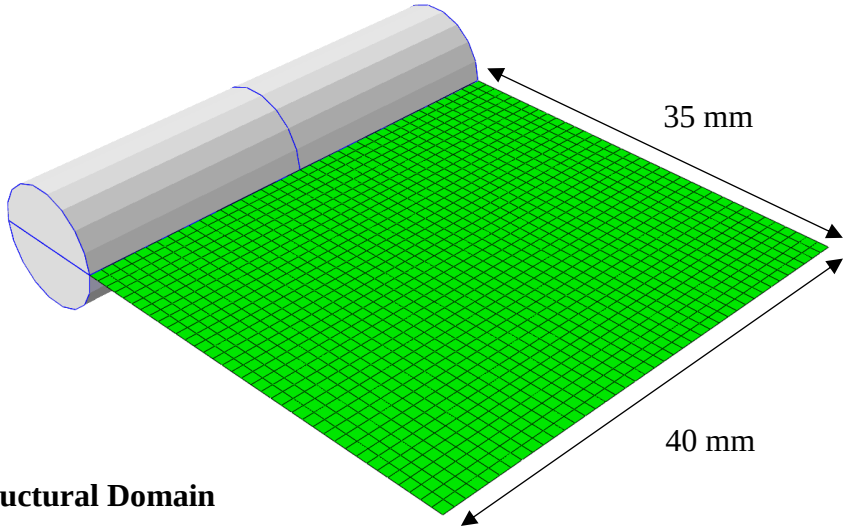


**Structural Domain**

Number of elements:1400

TRIAL 2

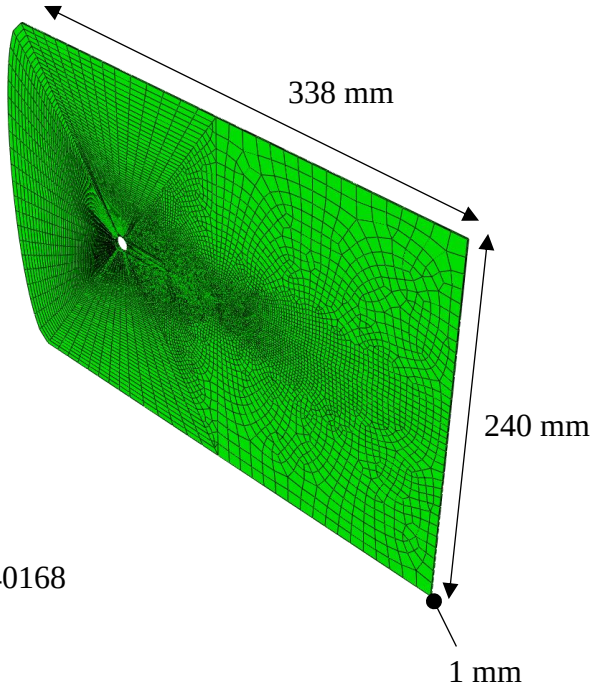


**Fluid Domain**

Number of elements: 40168

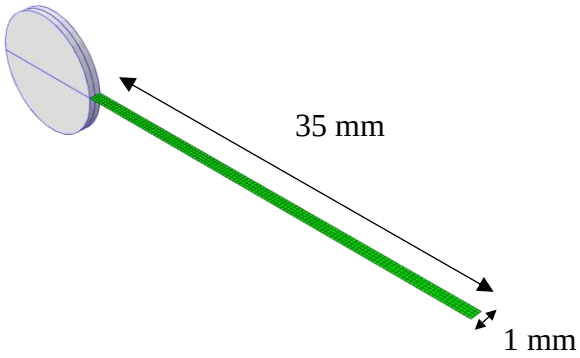


**Structural Domain**

Number of elements:468

## B. INPUT FILES

### Fluid Domain

```
*Heading
** Job name: jul25eve1-fluidD_z Model name: fluidD_z
** Generated by: Abaqus/CAE 6.14-2
*Preprint, echo=NO, model=NO, history=NO, contact=NO
**
** PARTS
**
*Part, name=fluid
*End Part
```

---

```
** ASSEMBLY
**
*Assembly, name=Assembly
**
*Instance, name=fluid-1, part=fluid
      -39.75,         -95.,         -0.5
*Node
** Nodal definition of parts and assembly omitted
**
** Section: Section-1
*Fluid Section, type=SINGLE FLUID, elset=Set-5
turek_july,
*End Instance
```

---

```
** MATERIALS
**
*Material, name=turek_july
*Density
 1e-09,
*Viscosity
 1e-06,
*Material, name=water
*Density
 1e-09,
*Viscosity
 1e-09,
**
** PREDEFINED FIELDS
**
** Name: Predefined Field-1   Type: Fluid turbulence
```

```
*Initial Conditions, type=TURBNU, Element Average
_PDF_WholeModel, 1e-09
```

---

```
** STEP: Step-1
**
*Step, name=Step-1, nlgeom=NO
*CFD, incompressible navier stokes
0.002, 40., 0.025, 1., 1
1e-15, 1.,  , 1., 1.

*Momentum Equation Solver
1000000, 2, 1e-10
*Pressure Equation Solver
1000, 2, 1e-10
ICC, 2, 2, FGMRES
*Transport Equation Solver
1000, 2, 1e-10
*Turbulence Model, type=SPALART ALLMARAS
0.1355, 0.622, 7.1, 5., 3.2391, 0.3, 2., 0.6667
0.41
0.8889,
```

---

```
** BOUNDARY CONDITIONS
**
** Name: cylin_bound Type: Fluid wall condition
*Fluid Boundary, type=Surface
cylinder_int, DIST, 0.
*Fluid Boundary, type=Surface
cylinder_int, VELX, 0.
cylinder_int, VELY, 0.
cylinder_int, VELZ, 0.
*Fluid Boundary, type=Surface
cylinder_int, TURBNU, 0.
** Name: d_cylin Type: Displacement/Rotation
*Boundary
cylin, 1, 1
cylin, 2, 2
cylin, 3, 3
** Name: d_ext Type: Displacement/Rotation
*Boundary
ext, 1, 1
ext, 2, 2
ext, 3, 3
** Name: d_symm Type: Displacement/Rotation
*Boundary
sym, 3, 3
** Name: inlet Type: Fluid inlet/outlet
*Fluid Boundary, type=Surface
inlet, VELX, 1000.
```

```
inlet, VELY, 0.
inlet, VELZ, 0.
** Name: outlet Type: Fluid inlet/outlet
*Fluid Boundary, type=Surface
outlet, P, 0.
** Name: symm Type: Fluid inlet/outlet
*Fluid Boundary, type=Surface
symm, VELZ, 0.
** Name: top_bot Type: Fluid inlet/outlet
*Fluid Boundary, type=Surface
top_bot, VELX, 1000.
top_bot, VELY, 0.
top_bot, VELZ, 0.
```

---

```
** LOADS
**
** Name: grav   Type: Gravity
*Dload
, GRAV, 9.81, 0., -1., 0.
** Interaction: fsi
*CONTROLS, TYPE=FSI, DISTORTION CONTROL=ON
,,,1.5
*Co-simulation, name=fsi, program=MULTIPHYSICS
*Co-simulation Region, import, type=SURFACE
fluid-1.seam, U
fluid-1.seam, V
*Co-simulation Region, export, type=SURFACE
fluid-1.seam, LUMPEDMASS
fluid-1.seam, TRSHR
```

---

```
** OUTPUT REQUESTS
**
*Restart, write, number interval=80
**
** FIELD OUTPUT: F-Output-1
**
*Output, field, time interval=0.001
*Node Output
DENSITY, PRESSURE, TURBEPS, TURBKE, U, V, VORTICITY
*Output, history, frequency=0
*End Step
```

## Solid Domain

```
*Heading
** Job name: jul25eve1-structD_z Model name: structD_z
** Generated by: Abaqus/CAE 6.14-2
*Preprint, echo=NO, model=NO, history=NO, contact=NO
**
** PARTS
**
*Part, name=Part-2
*Node
** Nodal definition of parts and assembly omitted
** Section: Section-1
*Shell Section, elset=whole, material=turek_july
2., 5
*End Part
```

---

```
** ASSEMBLY
**
*Assembly, name=Assembly
**
*Instance, name=Part-2-1, part=Part-2
          5.,           0.,         -0.5
*End Instance
**
*Instance, name=Part-3-1, part=Part-3
         20.,           0.,        -3.25
         20.,           0.,        -3.25,          19.,
0.,         -3.25,           90.
*End Instance
**
*Node
** Nodal definition of parts and assembly omitted
** Constraint: Constraint-1
*Display Body, instance=Part-2-1
*End Assembly
```

---

```
** MATERIALS
**
*Material, name=kapton
*Density
 1.42e-09,
*Elastic
49., 0.34
*Plastic
 69.,   0.
 90., 0.02
231., 0.69
```

```
*Material, name=mylar
*Density
 1.39e-09,
*Elastic
49., 0.38
*Plastic
100.,   0.
200., 1.16
*Material, name=rigid_mat
*Density
 7.8e-09,
*Elastic
 2e+08, 0.3
*Material, name=rubber
*Density
 1.36e-09,
*Elastic
16., 0.48
*Material, name=turek_july
*Density
 1e-09,
*Elastic
140., 0.4
**
```

---

```
** INTERACTION PROPERTIES
**
*Surface Interaction, name=IntProp-1
1.,
*Friction
0.,
*Surface Behavior, pressure-overclosure=HARD
**
** BOUNDARY CONDITIONS
**
** Name: fix Type: Symmetry/Antisymmetry/Encastre
*Boundary
Part-3-1.fix, ENCASTRE
** Name: z_prev Type: Displacement/Rotation
*Boundary
Part-3-1.whole, 3, 3
Part-3-1.whole, 4, 4
Part-3-1.whole, 5, 5
------------------------------------------------------------
------
**
** STEP: Step-1
**
*Step, name=Step-1, nlgeom=YES, inc=10000000
*Dynamic
40.,40.,1e-15
```

```
** Interaction: FSI
*Co-simulation, name=FSI, program=MULTIPHYSICS
*Co-simulation Region, import, type=SURFACE
fsi_surf, CF
fsi_surf, LUMPEDMASS
*Co-simulation Region, export, type=SURFACE
fsi_surf, U
fsi_surf, V
```

---

```
** CONTROLS
**
*Controls, reset
*Controls, analysis=discontinuous
*Controls, parameters=time incrementation
, , , , , , , , , ,
0.5, 0.75, 0.8, 0.7, 0.5, 0.5, ,
```

---

```
** OUTPUT REQUESTS
**
*Restart, write, number interval=80, time marks=NO
**
** FIELD OUTPUT: F-Output-4
**
*Output, field
*Node Output
A, U, V
*Element Output, directions=YES
E, LE, S
**
** HISTORY OUTPUT: H-Output-1
**
*Output, history, variable=PRESELECT
*End Step
```

## Co-Simulation Engine (Coupling Module)

```
*include,input=jul25eve1-fluidD_z.inp
*include,input=jul25eve1-structD_z.inp
*include,input=jul25eve1_config.xml
```